ELSEVIER

Tectonophysics 359 (2002) 225–253

TECTONOPHYSICS

www.elsevier.com/locate/tecto

Cretaceous–Cenozoic history of the southern Tan-Lu fault zone: apatite fission-track and structural constraints from the Dabie Shan (eastern China)

J.C. Grimmer[a], R. Jonckheere[a,b], E. Enkelmann[a,b], L. Ratschbacher[a,*], B.R. Hacker[c], A.E. Blythe[d], G.A. Wagner[b], Q. Wu[e], S. Liu[e], S. Dong[f]

[a]*Institut für Geologie, Technische Universität Bergakademie Freiberg, Bernhard von Cottastrasse 2, D-09599 Freiberg Sachsen, Germany*
[b]*Max-Planck-Institut für Kernphysik, D-69117 Heidelberg, Germany*
[c]*Department of Geology, University of California, Santa Barbara, CA, USA*
[d]*Department of Earth Sciences, University of Southern California, Los Angeles, CA, USA*
[e]*Changsha Institute of Geotectonics, Changsha, PR China*
[f]*Chinese Academy of Geological Sciences, 100037 Beijing, PR China*

Received 15 November 2001; accepted 12 August 2002

Abstract

Apatite fission-track (AFT) and structural data outline the Late Cretaceous – Cenozoic history of the southern Tan-Lu fault zone (TLFZ), one of Asia's major faults, the Triassic–Jurassic Dabie orogen, Earth's largest track of ultrahigh-pressure rock exposure, and its foreland, the Yangtze foreland fold-thrust belt. The fission-track analyses utilized the independent (ϕ-), Z- and ξ-methods for age determination, which yielded within error identical ages. Ages from Triassic–Jurassic syn-orogenic foreland sediments are younger than their depositional age and thus were reset. A group of ages records rapid cooling following shallow emplacement of granitoids of the widespread latest Jurassic – Early Cretaceous "Yanshanian" magmatism. Most ages are 90 to 55 Ma and document cooling following reheating at 110–90 Ma, the time when the basement units of the Dabie Shan were last at >200 °C. This cooling coincides with rifting marked by the Late Cretaceous – Eocene red-bed deposition in eastern China. During this period, the Dabie basements units exhumed in the footwall of the Tan-Lu fault with the Qianshan basin in the hanging wall; the associated stress field is transtensional (NW-trending principal extension direction). The youngest fission-track ages and temperature–time path modeling point to enhanced cooling in the footwall of the Tan-Lu and associated faults at 45 ± 10 Ma. The related stress field is transtensional, with the principal extension direction changing trend from NW to W. It may be the far-field expression of the India–Asia collision superposed on the back-arc extension setting in eastern China. A regional unconformity at ~ 25 Ma marks an upper bound for the inversion of the Late Cretaceous – Eocene rift structures. During the Neogene, further subsidence in the eastern China basins was accommodated by sub-horizontal NE–SW extension, and followed by the presently active NW–SE extension. The Tan-Lu fault along the eastern edge of the Dabie Shan had normal

---

[*] Corresponding author. Tel.: +49-3731-393758; fax: +49-3731-393597.
E-mail address: lothar@geo.tu-freiberg.de (L. Ratschbacher).

PII: S0040-1951(02)00513-9

and then sinistral-transpressive motion during the Late Cretaceous – Eocene. Its motion changed during the Neogene from sinistral transtensive to normal and then to its present dextral transtensive activity.

Keywords: Tan-Lu fault zone; Apatite fission-track thermochronology; Fault-slip analysis; Late Cretaceous–Cenozoic tectonics; Dabie Shan

1. Introduction

Several >100.000 km^2 rift basins paralleling the Pacific margin testify to significant Cretaceous – Cenozoic extension in eastern Asia (Fig. 1). Their evolution is commonly assigned to Pacific subduction and back-arc extension (e.g. Northrup et al., 1995) and to lateral extrusion of eastern Asia due to the India–Asia collision (e.g. Tapponnier and Molnar, 1977; Zhang et al., 1995). The 'Tan-Lu' is a major NNE-striking fault zone (TLFZ), which bounds several of these basins (Fig. 1). It stretches more than 1000 km sub-parallel to the Pacific margin in China, likely extends into Russia (e.g. Xu and Zhu, 1995), and has been assigned key significance for the tectonic evolution of eastern Asia; for example, its apparent offset of the Dabie-Sulu ultrahigh-pressure (UHP) orogen (Fig. 1) has sparked discussion of its role during the exhumation of these unusual rocks (e.g. Yin and Nie, 1993). Proterozoic, Paleozoic, Triassic–Jurassic, and Cretaceous radiometric ages have been reported from the TLFZ (e.g. Fletcher et al., 1995; Chen et al., 1989b; Dou et al., 1996; Xu and Zhu, 1995), but whether all these ages date fault activity is questionable.

Cretaceous and Cenozoic structures dominate the orogenic architecture of the Triassic – Jurassic UHP Dabie belt and contributed to its exhumation from ≤ 30 km depth (Ratschbacher et al., 2000). Cretaceous magmatic crustal recycling and heating (>250 to >700 °C) were most prominent in northern Dabie (Northern Orthogneiss Unit), and exhumation, magmatism, and cooling were controlled by Cretaceous transtension dated at 140–120 Ma. The onset of crustal extension was preceded by a reheating of the Dabie crust (~ 140 Ma) coeval with the onset of voluminous magmatism in eastern China (~ 145 Ma). The entire Dabie Shan cooled to < 250 °C by ~ 115 Ma but its eastern part along the TLFZ was reheated to >200 °C at 110–90 Ma. The Tan-Lu continental-scale fault zone was a normal fault in the mid-Cretaceous (~ 110–90 Ma), and underwent ≥ 5.4 km of dip slip and ≥ 4 km throw in the Cenozoic (Ratschbacher et al., 2000); the most prominent Cenozoic structure besides the TLFZ is the active Jinzhai fault zone in northernmost Dabie (Fig. 2).

This study focuses on the Cretaceous – Cenozoic tectonic and low-temperature history along the southern TLFZ and associated faults at the eastern edge of Dabie Shan and in the Yangtze foreland fold-thrust belt (YFTB; Figs. 1 and 2). First, we establish regional stress fields, which reflect distinct regional deformation events; these fields were derived from a regional analysis of mesoscale fault-slip data and an evaluation of map-scale structural geometries. Second, we discuss the value of three apatite age standards and utilize three methods to derive apatite fission-track (AFT) ages for the magmatic, metamorphic, and sedimentary rocks straddling the southern TLFZ. Third, we critically discuss the $T[t]$-path modeling of our samples. Finally, we integrate the regional stress-field estimates with the AFT data and the evolution of Late Cretaceous – Cenozoic basins and place the TLFZ, the adjacent Dabie Shan, and the YFTB into a Cretaceous – Cenozoic eastern Asian tectonic framework. We thus provide tectonothermal data on one of Earth's largest fault zones and the late-stage exhumation history of the world's largest track of UHP exposure.

2. Structural analysis

Our geometric, kinematic, and dynamic data are summarized in Figs. 3–6 and Table 1. They are based on fieldwork, re-evaluation of the 1:200.000 and 1:500.000 geological maps of the Geological Surveys of Anhui, Jiangxi, and Hubei (R.G.S. Anhui, 1975, 1987; R.G.S. Hubei, 1990), and integration of the data

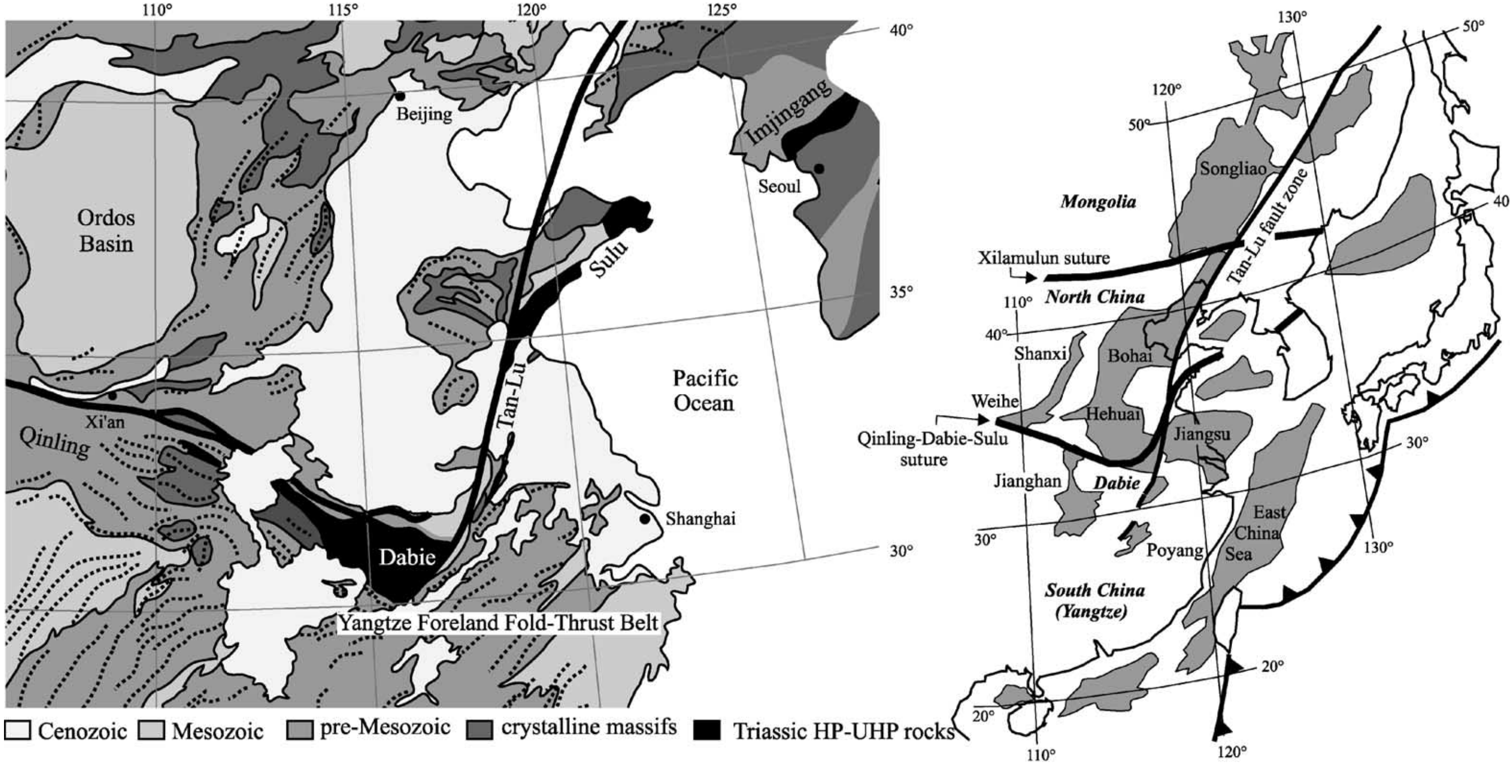

Fig. 1. Left: The Triassic–Jurassic ultrahigh-pressure Qinling–Dabie–Sulu orogen in eastern China, the Yangtze foreland fold-thrust belt, and the Tan-Lu fault zone (modified from Hacker et al., 2000). Dotted lines indicate trends of major fold trains. Right: Cenozoic basins in eastern China (modified from Allen et al., 1997; Chen and Qin, 1989).

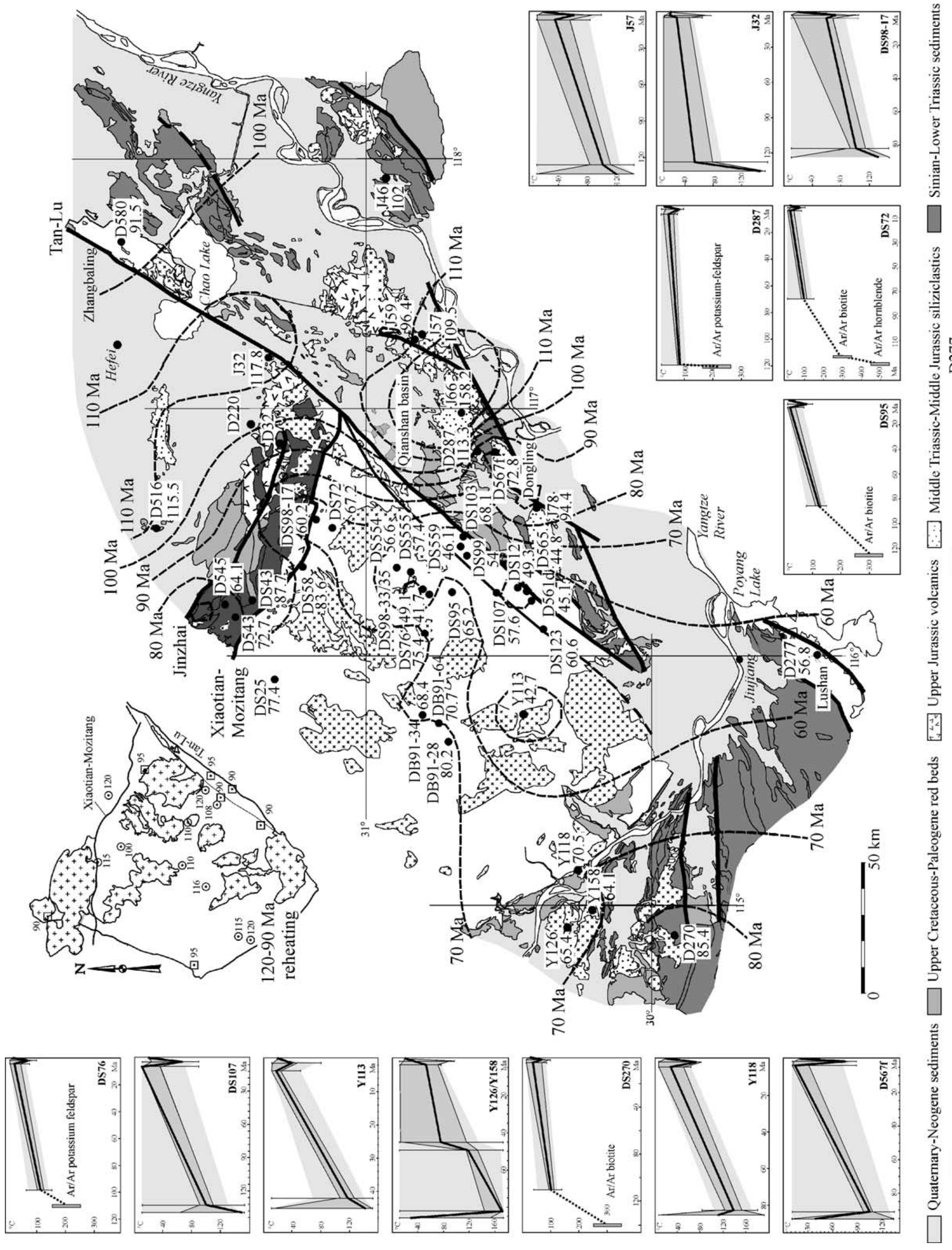
Tan-Lu
Zhangbaling
Hefei
Chao Lake
Yangtze River
Qianshan basin
Dongling
Jinzhai
Xiaotian-Mozitang
Poyang Lake
Jiujiang
Lushan
120-90 Ma reheating
N
31°
30°
115°
116°
117°
118°
50 km
0
60 Ma
70 Ma
80 Ma
90 Ma
100 Ma
110 Ma
D580 91.5
J46 102
J59 96.4
J57 109.5
J32 117.8
D220
D516 115.5
D287 113.3
D166 158.2
D567f 72.8
D178 94.4
DS98-17 60.2
DS72 67.2
DS545 64.1
DS43 87.7
D543 72.7
DS58 83.6
DS554 56.6
DS555 57.4
DS559 46.1
DS103 68.1
DS99 54
DS127 49.3
D565 44.8
D561 45.1
DS107 57.6
DS123 60.6
DS95 65.2
DS98-33/35
DS76 75.4
DB91-34 68.4
DB91-64 70.7
DB91-28 80.2
DS25 77.4
Y113 42.7
Y118 70.5
Y158 64.1
Y126 65.4
D270 85.4
D277 56.8
Ar/Ar potassium feldspar
Ar/Ar biotite
Ar/Ar hornblende
°C
Ma
DS76
DS107
Y113
Y126/Y158
DS270
Y118
D567f
DS95
D287
DS72
J57
J32
DS98-17
Quaternary-Neogene sediments
Upper Cretaceous-Paleogene red beds
Upper Jurassic volcanics
Middle Triassic-Middle Jurassic siliziclastics
Sinian-Lower Triassic sediments
Granitoids
Foziling/Luzhenguang greenschists/amphibolites
Crystalline basement
Fault
Age contours
D277 56.8 Sample number and apatite fission track age

published by Ratschbacher et al. (2000), Zhang et al. (1999), and Schmid et al. (1999). Appendix A summarizes our approach to fault-slip analysis and definition of stress-tensor groups in the brittle crust and reviews the applied calculation techniques. The computer-program package of Sperner et al. (1993) was employed to calculate principal stress axes ($\sigma_1 \geq \sigma_2 \geq \sigma_3$). These axes are interpreted to represent stress fields during different regional deformation events (e.g. Angelier, 1984). Critical to the establishment of the stress fields is the recognition of consistent superposition criteria between fault subsets on a regional scale. Besides using classic overprinting relationships, we carefully investigated the pre- and post-folding attitudes of faults and related striae. For example, at many locations we observed a characteristic fault set that is sub-normal to bedding and has striae sub-parallel to the bedding-fault intersection. This set is interpreted to represent sub-horizontal compression by strike-slip faulting prior to folding. The "relative chronology matrix" in Fig. 3a summarizes for the Late Cretaceous – Cenozoic the number of subsets for which geologic overprinting criteria constrain a relative age sequence and thus documents a deformation history in terms of superposed regional stress fields. The upper right triangle of the matrix contains all subset chronologies consistent with the available overprinting criteria, the lower left triangle those incompatible with the chosen subdivision. Except for the oldest subset, no incompatibilities occur, indicating that the sequence of stress fields, schematically illustrated in Fig. 3b with the most common faults, is reliable, based on the available stations. Fig. 3c depicts fault subsets, characteristic of the five events of the Late Cretaceous – Cenozoic deformation history.

2.1. Early Cretaceous deformation

Latest Jurassic – Early Cretaceous structures in the Dabie Shan are dominantly normal and strike-slip shear zones and faults; by far the highest strain was accommodated during an initial ductile flow event (Ratschbacher et al., 2000). The major crust-shaping event was the formation of the magmatic–metamorphic–structural dome of the Northern Orthogneiss Unit (Fig. 4) under NW–SE sub-horizontal extension and sub-vertical and subordinate NE–SW contraction during activation of the Xiaotian-Mozitang detachment fault (XMF; Fig. 2). The characteristic regional feature is a clockwise change in the orientation of the sub-horizontal stress axes; that is, the trend of the principal extension direction changed from early NW to intermediate N to late NE. Ductile flow is well dated in Dabie by pre- to syn-tectonic orthogneisses with U/Pb zircon ages of 137 to 128 Ma and post-tectonic (undeformed) granitoids of 129 to 125 Ma. ^{40}Ar/^{39}Ar thermochronology indicates that most of Dabie cooled below 250 °C by ~ 115 Ma, coeval with brittle–ductile and brittle faulting (Ratschbacher et al., 2000).

In the YFTB, mafic dikes and basement domes manifest crustal extension (Schmid et al., 1999; Lin et al., 2000). Dating of one of these dikes (sample A179; Fig. 4; NE-trending after unfolding) by the whole rock K–Ar method yielded 135 ± 5 Ma (Table 2); it thus predates the change from NW to NE extension and later folding. Dongling and Lushan are the most prominent basement domes and expose upper- to mid-crustal rocks of the Proterozoic Yangtze crystalline basement (Fig. 4). In Lushan, a NW–SE extension occurred between Permian and Early Cretaceous, and N–S to dominantly NE–SW transtension (with a strong sub-horizontal NE-trending stretching lineation and open folds with axes parallel to the lineation) is syn- to post-tectonic to the ~ 127 Ma Haihui granodiorite (Lin et al., 2000). In Dongling, we obtained an ^{40}Ar/^{39}Ar age of 124.8 ± 1.2 Ma (D567d; Fig. 8, Table 2) from white mica that defines the NE-trending stretching lineation (Fig. 4) and is thus interpreted to be syn-kinematic. In aggregate, the data from Dabie, Lushan, and Dongling indicate that the characteristic regional clockwise change in the orientation of the sub-horizontal strain/stress fields, from early NW–SE to late NE–SW transtension, occurred between ~ 140 and ~ 115 Ma; the latter stress field was established after ~ 127 Ma.

Fig. 2. Center: Tectonostratigraphic map of the Dabie Shan and the Yangtze foreland fold-thrust belt showing sample locations of apatite fission-track ages. Age contours were generated using a kriging method. The youngest ages occur in the footwall of the Tan-Lu fault zone. Temperature–time path diagrams give preferred modeling solutions. Upper-left map shows mid-Cretaceous ^{40}Ar/^{39}Ar potassium-feldspar reheating ages (Ma) in Dabie (modified from Ratschbacher et al., 2000).

Table 1
Location of stations and parameters of the deviatoric stress tensor

Station	Stratigraphy–lithology	Latitude	Longitude	Method	*N*	σ_1	σ_2	σ_3	*R*	*F*
Late early Cretaceous stress field										
D516a	K_1 sandstone	31°43′08″	116°30′35″	NDA	04/04	325 13	154 77	055 02	0.4	22°
D567-3	K_1 marble	30°33′50″	116°49′11″	NDA	04/04	152 22	357 66	246 09	0.5	05°
D569-1	J_{1-2} graywacke	30°40′18″	116°53′02″	NDA	15/15	135 14	288 75	044 07	0.5	23°
D574a	J_3 volcanics	30°58′07″	117°25′42″		03/03	329 03		239 11		
J24-1ro	J_3 volcanics	31°20′24″	117°04′31″	NDA	04/04	317 02	069 84	227 06	0.5	08°
J24-2ro				NDA	07/07	285 01	021 84	195 06	0.6	05°
J33-1	J_3 basalt	31°12′09″	117°15′27″	NDA	05/05	290 10	114 80	020 01	0.6	11°
J73arot	K_1 marble, monzonite	30°33′25″	116°53′17″	NDA	13/13	336 03	108 85	246 04	0.6	19°
J73brot				NDA	08/08	304 17	116 73	214 02	0.6	19°
Y100-2	T_1 limestone	29°53′00″	115°30′00″	NDA	05/05	292 20	104 70	201 03	0.5	15°
Y162-1	T_1 limestone	29°47′51″	115°35′51″		03/03	328 07	129 83	237 02	0.5	17°
Late Cretaceous–Paleogene stress field										
D514-3	K_1 red beds	32°15′21″	117°52′20″	NDA	04/04	352 03	088 66	261 24	0.5	19°
D569-4	J_{1-2} graywacke	30°40′18″	116°53′02″	NDA	04/04	049 19	210 70	317 06	0.5	09°
D572Ka	K_2–E red beds	30°45′20″	117°54′48″	NDA	17/17	061 01	160 81	331 09	0.5	11°
D572Kb				NDA	05/05	193 03	285 31	098 59	0.5	06°
D574b	J_3 volcanics	30°58′07″	117°25′42″	NDA	07/07	001 14	109 51	260 36	0.5	12°
J33b	J_3 basalt	31°12′09″	117°15′27″	NDA	04/04	001 09	098 41	261 48	0.5	13°
J4043c	T_1 limestone	30°57′42″	118°06′29″	NDA	11/11	217 03	322 77	126 13	0.4	12°
J48a	T_1 limestone	30°49′35″	117°47′22″	PBT	04/04	233 30	020 55	133 16		
J61-3	T_1 limestone	30°40′31″	117°06′33″	NDA	05/05	185 11	308 70	091 17	0.6	13°
J78b	J_2 graywacke	30°24′18″	116°36′30″	NDA	10/10	063 21	289 61	161 19	0.4	12°
Y100-3	T_1 limestone	29°53′00″	115°30′00″	NDA	09/09	045 09	160 70	312 18	0.5	08°
Y126-1	J_2 graywacke	30°18′14″	114°57′08″	NDA	06/06	205 05	329 81	114 07	0.7	14°
Y129-2	J_2 graywacke	30°16′56″	114°59′21″	NDA	04/04	226 14	009 73	133 10	0.5	08°
Y136-2	J_1 sandstone	30°13′50″	115°03′08″	NDA	04/04	236 10	353 68	143 19	0.5	11°
Y138-1r	J_3 volcanics	30°16′21″	115°01′14″	NDA	08/08	207 17	027 73	123 03	0.6	11°
Y138-2				NDA	10/10	037 15	245 73	129 07	0.6	13°
Y138-3				NDA	04/04	174 15	323 73	082 08	0.6	16°
Y141-2	K_1 volcanics	29°59′40″	114°43′03″		03/03	020 16		289 01		
Y145-1	T_2 dolomite	30°03′33″	114°55′39″	NDA	08/08	050 24	217 65	318 05	0.5	13°
Y147-2	T_2 dolomite	30°04′13″	114°59′44″	PBT	04/04	061 13	248 77	152 01		
Y151-1	K_2–E red beds	29°52′43″	115°05′39″	NDA	06/06	211 02	115 68	302 22	0.7	08°
Y151-2					03/03	352 15		259 10		
Y153-1	K_2–E basalt			PBT	04/04	065 11	254 79	155 02		
Y158-1	T_2 sandstone	30°14′34″	115°00′59″	NDA	09/09	029 04	240 85	119 02	0.5	11°
Y162-2	T_1 limestone	29°47′51″	115°35′51″	PBT	07/07	232 13	074 76	323 05		
Late Oligocene–Neogene stress field										
D514-5	K_1 arkose	32°15′21″	117°52′20″	NDA	05/05	264 03	165 71	355 19	0.5	15°
D514-6				NDA	04/04	043 86	309 00	219 04	0.5	09°
D516b	K_1 sandstone	31°43′08″	116°30′35″	NDA	09/09	150 71	341 19	250 03	0.5	16°
D516c				NDA	19/19	226 72	035 18	126 03	0.6	17°
D567-4	K_1 marble	30°33′50″	116°49′11″	NDA	10/10	203 63	306 07	040 26	0.5	08°
D569-5	J_{1-2} graywacke	30°40′18″	116°53′02″	NDA	04/04	203 72	316 07	048 16	0.5	01°
D569-6				NDA	12/12	074 79	228 10	319 05	0.5	13°
D574c	J_3 volcanics	30°58′07″	117°25′42″	NDA	05/05	034 85	152 02	242 04	0.6	10°
J51d	T_1 limestone	30°54′25″	117°35′47″	NDA	07/07	210 66	056 22	322 10	0.4	12°
J71c	J_1 graywacke	30°40′23″	116°52′59″	NDA	06/06	082 11	203 69	349 18	0.5	07°
J71d					03/03	296 80		043 03		
Y126-3	J_2 graywacke	30°18′14″	114°57′08″	NDA	07/07	051 76	209 13	300 05	0.6	11°

Table 1 (*continued*)

Station	Stratigraphy–lithology	Latitude	Longitude	Method	N	σ_1	σ_2	σ_3	R	F
Late Oligocene–Neogene stress field										
Y138-4	J_3 volcanics	30°16′21″	115°01′14″	NDA	08/08	083 05	328 79	174 10	0.6	20°
Y141-3	K_1 volcanics	29°59′40″	114°43′03″	NDA	14/14	074 11	189 66	339 21	0.6	15°
Y141-4					02/02	044 84		240 06		
Y141-5				NDA	11/11	044 58	220 32	311 02	0.6	09°
Y147-4	T_1 limestone	30°04′13″	114°59′44″	PBT	06/06	156 77	327 13	058 02		
Y150	E conglomerates	29°54′31″	115°10′34″							
Y152-3	T_1 limestone	29°46′24″	115°13′55″	PBT	05/05	257 13	068 77	167 02		
Y152-5				PBT	04/04	033 72	220 18	129 02		
Y162-4	T_1 limestone	29°47′51″	115°35′51″		03/03	205 77		67 10		
Y164-4	T_1 limestone	29°37′05″	115°38′04″	PBT	04/04	204 69	051 19	318 09		

The numerical dynamic analysis method (NDA; Spang, 1972) and the P–B–T axes method (PBT; Turner, 1953) were used for calculation of principal stress directions ($\sigma_1 \geq \sigma_2 \geq \sigma_3$). For stations with less than four fault-slip data, we report visually estimated contraction and extension directions. In the measurement column (N), first number is number of measurements used for calculation, second number gives total number of measurements. For σ_1–σ_3, azimuth (first number) and plunge (second number) of the principal stress axes are given. The stress ratio R is $(\sigma_2 - \sigma_3)(\sigma_1 - \sigma_3)^{-1}$ (where 1 is uniaxial confined extension, 0 is uniaxial confined compression). The fluctuation F gives the average angle between the measured slip and the orientation of the calculated theoretical shear stress. $T_{1,2}$: Early, Middle Triassic; $J_{1,2,3}$: Early, Middle, Late Jurassic, $K_{1,2}$: Early, Late Cretaceous, E: Eocene.

Fig. 4 integrates the available local stress orientations for the NE–SW transtension within and around Dabie, complementing the compilation for the earlier NW–SE transtension presented by Ratschbacher et al. (2000). Our structural analysis in the YFTB documents Triassic regional folding overprinted by NW–SE shortening and NE–SW extension (Fig. 4, Table 1) manifested by faulting and gentle folding of Jurassic strata (Schmid et al., 1999). The southern TLFZ was probably not active during the Early Cretaceous for the following reasons: (1) During NW–SE transtension, the TLFZ should have been a normal fault zone with Early Cretaceous deposits in the hanging wall; such sediments do not occur east of the TLFZ or in the eastern YFTB. In contrast, Early Cretaceous sediments up to several kilometers thick in the foreland north of Dabie (Han et al., 1989) testify to significant activity along the XMF and related faults. (2) Cooling in Dabie shows a structural control by the XMF, across which the sharpest cooling gradient occurs; in contrast, no such influence on cooling rates has been documented across the TLFZ (Ratschbacher et al., 2000).

2.2. Late Cretaceous–early Cenozoic deformation

Overprinting criteria establish two consecutive Late Cretaceous–early Cenozoic stress fields (Table 1, Figs. 3 and 5). The kinematic interpretation of map-scale faults in Fig. 5 is based on stress field 1 (see below).

Stress field 1 (Fig. 5): Fault sets in Upper Cretaceous–Eocene (K_2–E) red beds (e.g. station Y151) that contain faults sub-normal to bedding and striae sub-parallel to the bedding-fault intersection lineation are interpreted to reflect sub-horizontal compression by strike-slip faulting prior to folding. Fault inversion establishes NE–SW compression and NW–SE extension (σ_1: 045 ± 20°, σ_3: 135 ± 20°, 16 stations). The red beds were mainly deposited in half grabens (e.g. Qianshan, Poyang basins, Fig. 5). There may be a pull-apart basin south of Dabie (stations Y151, Y153, Y100, Y162, Fig. 5). In this stress field, Paleogene(?) basalts (Zheng, 1985) were emplaced as sills in the red beds (station Y153). Distinct accessory biotite identifies these basalts as the source of hematite-encrusted basalt pebbles in karst breccia of Triassic carbonates; the widespread karstification in the YFTB is thus Tertiary. The major active faults were the TLFZ and the fault zones bounding the Dongling and Lushan domes against the Yangtze river depression and the Poyang basin, respectively (see also Lin et al., 2000).

Stress field 2 (Fig. 5, gray-underlain plots): N–S compression (σ_1: 182 ± 18°, 8 stations) is recorded in K_2–E red beds along the TLFZ, making it a sinistral transpressive fault (e.g. stations D572, Y138, Y141,

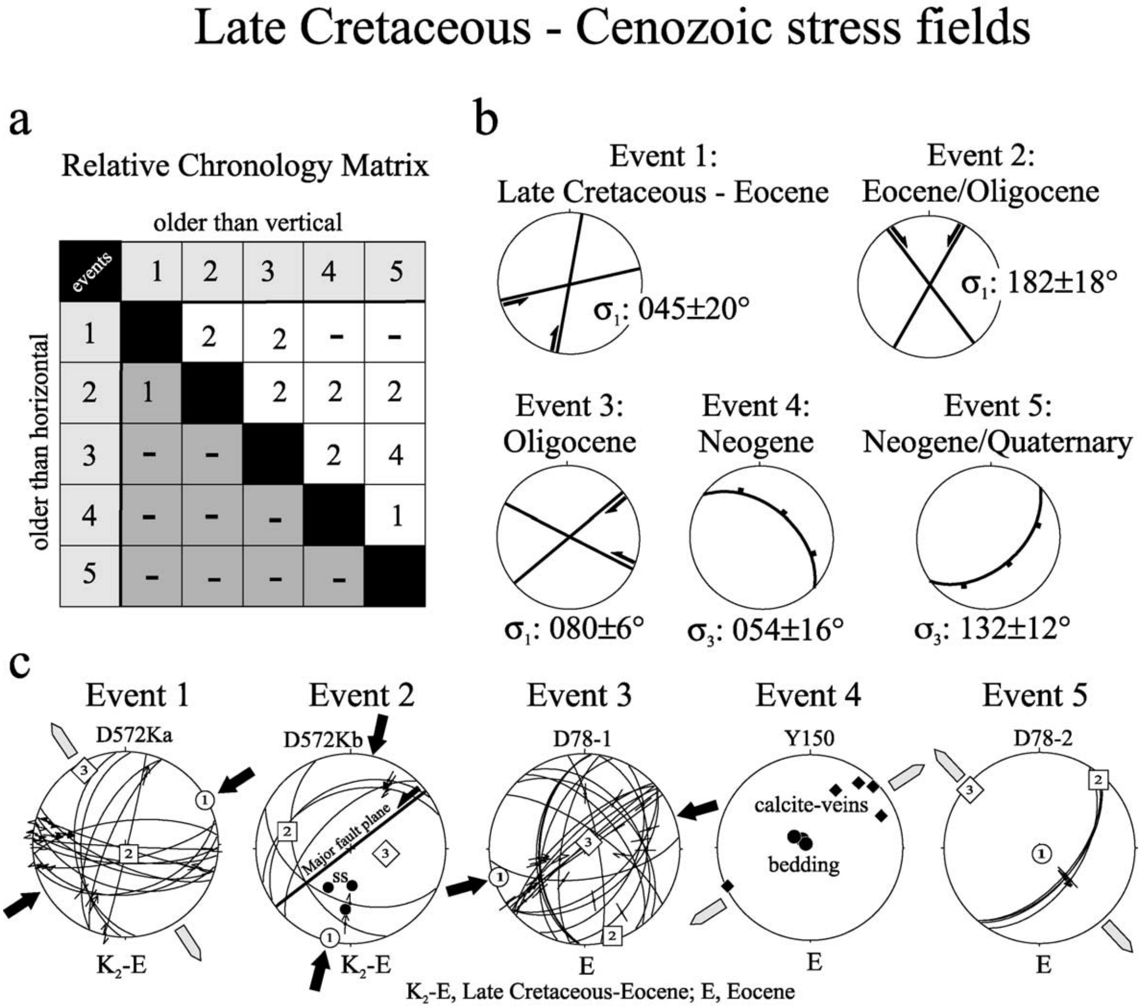

events	1	2	3	4	5
1		2	2	-	-
2	1		2	2	2
3	-	-		2	4
4	-	-	-		1
5	-	-	-	-	

Fig. 3. (a) The "relative chronology matrix" summarizes the number of subsets for which geologic overprinting criteria constrain a relative age sequence and thus sets up the deformation history plotted as "events" in terms of superposed regional stress fields. In this matrix, rows correspond to the older event, and columns correspond to the younger one. The upper right triangle of the matrix contains all chronologies consistent with the classification adopted, whereas the lower left triangle is the domain of incompatibility. (b) Summary of Late Cretaceous – Cenozoic events (stress fields) in Dabie and the Yangtze foreland fold-thrust belt highlighted by the trends of major faults, principal compression or extension directions, and age. (c) Field examples from Late Cretaceous–Eocene red beds for (b); station D78 is from Ratschbacher et al. (2000). Stereograms (lower hemisphere, equal-area) are as follows. Faults are drawn as great circles and striae are drawn as arrows pointing into the direction of displacement of the hanging wall. Confidence level of slip-sense determination is expressed in the arrowhead style: solid, certain; open, reliable; half, unreliable; without head, poor.

Y151). Station D572 represents a sinistral transpressive, map-scale fault, which reactivated a normal fault (stress field 1) with K_2–E red beds in the hanging wall. The deformation here is end-Eocene or younger as the Eocene red beds are tilted northward. Stress field 2 was also recorded in Dabie (Ratschbacher et al., 2000).

2.3. Late Cenozoic deformation

Overprinting criteria establish three consecutive stress fields (Table 1, Figs. 3 and 6). The kinematic interpretation of map-scale faults in Fig. 6 is based on stress field 5 (see below).

Stress field 3 (Fig. 6): Five stations indicate a dextral reactivation of faults parallel to the TLFZ; σ_1 trends 080 ± 6°. This field was also recorded in Dabie (Ratschbacher et al., 2000).

Stress field 4 (Fig. 6, gray-underlain plots): Spectacular zones of multiply filled, up to 7-m-wide calcite veins (e.g. Y150) and associated normal faults in Eocene conglomerates testify to significant NE–SW extension (σ_3: 054 ± 16°, 9 stations). Locally, fault breccia (e.g. Y147) in pre-Upper Cretaceous rocks involve red beds even outside the present outcrop range of those rocks pointing to a formerly widespread K_2–E coverage. Early Neogene NE–SW extension was also documented in the Weihe graben of central China (north of the Qinling and part of the Shanxi rift system), the TLFZ, the Dabie basement, and North Vietnam (Bellier et al., 1991; Zhang et al., 1999; Ratschbacher et al., 2000; Jolivet et al., 1999).

Stress field 5 (Fig. 6, dark-gray-underlain plots): Active faults are currently forming under general NW–SE extension (σ_3: 132 ± 12°, 7 stations). The TLFZ is a dextral transtensional fault and the Jinzhai fault along northern Dabie fault is sinistral; the onset of faulting was likely late Miocene/Pliocene (Bellier et al., 1991; Zhang et al., 1995, 1999; Ratschbacher et al., 2000). Locally, curving slickenline fibers indicate a continuous clockwise change from the NE-oriented extension of the Neogene to the Recent SE-oriented extension.

3. Apatite fission-track results

Forty samples from sedimentary, metamorphic, and magmatic rocks of the Dabie Shan and YFTB were selected for AFT analysis. Appendix B details methodical and technical aspects, including the calculation and comparison of AFT ages obtained by the independent (ϕ-), Z- and ξ-methods, the evaluation of the Durango, Fish Canyon, and Mt. Dromedary standards, and our approach to $T[t]$-path modeling. Fig. 2 depicts the regional distribution of AFT ages and the preferred $T[t]$-paths. Radial plots (Galbraith, 1990) show extra-Poisson scatter in some cases, but do not indicate the presence of more than one age component.

The oldest age (158.2 ± 14.3 Ma), a Middle Triassic sandstone (J66), is younger than the depositional age. It remains unresolved whether this resulted from complete resetting before the time dated by the AFT age or partial resetting due to burial or advective heating at a later time, because no confined track lengths could be measured.

The next oldest ages are 117.8 ± 3.7 Ma (J32), 113.3 ± 3.6 Ma (D287), and 115.5 ± 6.7 Ma (D516). J32 is an undeformed subvolcanic syenite of presumed Early Cretaceous age. It has a narrow unimodal length distribution with the longest mean length (14.0 μm) of all samples (Fig. 7a–a). Despite the low number of confined tracks (N=36), the $T[t]$-path is well constrained, with rapid cooling through the partial annealing zone (PAZ), starting between ~ 135 and ~ 117 Ma, followed by a prolonged residence at lower temperatures. Whether the latter phase involved further slow cooling (< 1 °C/Ma) or no cooling depends on the timing of the first, rapid cooling phase (Fig. 7a–b, a–c). D287 is from a granitoid intrusion with an $^{40}Ar/^{39}Ar$ potassium-feldspar age of 120 ± 2 Ma (Table 2, Fig. 8). Although its fission-track age is similar to that of J32, its track length distribution is broader (Fig. 7b–a), with a shorter mean length (12.6 μm). Its $T[t]$-path is well constrained (N=108), and continuous-cooling type solutions provide a good fit. The onset of effective track accumulation took place before ~ 127 Ma, which is compatible with the potassium-feldspar age. The closeness of both ages suggests rapid cooling at around ~ 120 Ma. Because there is a component of shorter tracks, other types of $T[t]$-path, involving a change of cooling rate or thermal high around 110 Ma are also in agreement with the AFT data (Fig. 7b–c). These solutions place the start of effective track accumulation well before 120 Ma, and are not considered realistic. Both plutons intruded the volcano-sedimentary cover (J32 into Upper Jurassic volcanics; D287 into Lower Triassic carbonates); thus, the rapid cooling around ~ 120 Ma likely reflects cooling after intrusion. D516 is a Lower Cretaceous sandstone from the northern foreland. If it was derived from Dabie source rocks with ages similar to J32 and D287, erosion, transport, and sedimentation must have been rapid, and it was not exposed to elevated temperatures. This is supported by detrital potassium-feldspar ages from Upper Cretaceous and Paleogene red beds (Fig. 2; D32, D220, respectively), indicating that their source was dominated by rocks cooling through ~ 200 °C at 123 ± 1 to 119 ± 1 Ma (Hacker et al., 2000).

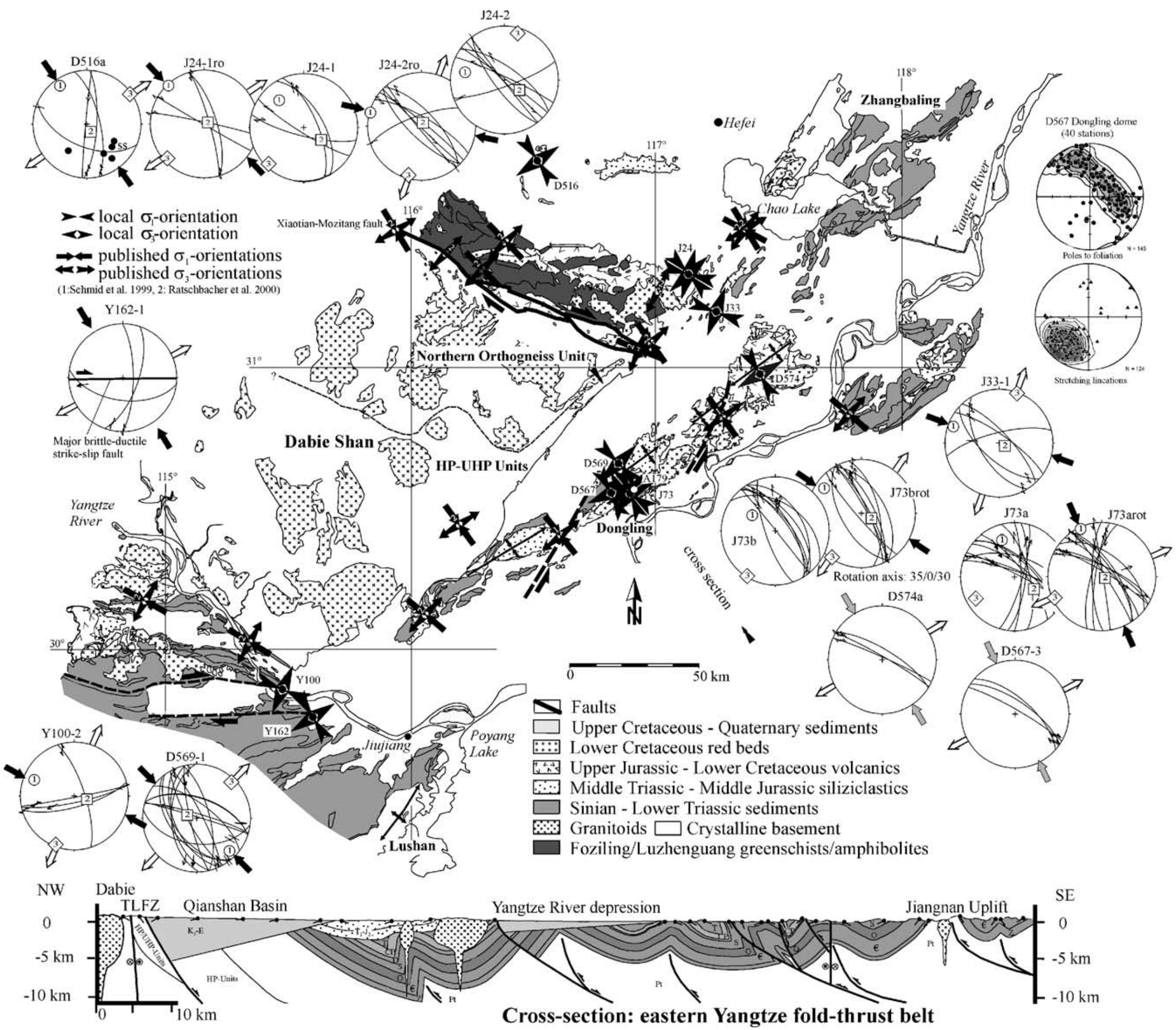
D516a
J24-1ro
J24-1
J24-2ro
J24-2
local σ1-orientation
local σ3-orientation
published σ1-orientations
published σ3-orientations
(1:Schmid et al. 1999, 2: Ratschbacher et al. 2000)
Y162-1
Major brittle-ductile strike-slip fault
Xiaotian-Mozitang fault
D516
Hefei
Zhangbaling
Chao Lake
Yangtze River
J24
J33
D574
Northern Orthogneiss Unit
Dabie Shan
HP-UHP Units
D569
D567
J73
Dongling
cross section
Yangtze River
Y100
Y162
Jiujiang
Poyang Lake
Lushan
Y100-2
D569-1
D567 Dongling dome (40 stations)
Poles to foliation
Stretching lineations
J33-1
J73b
J73brot
J73a
J73arot
Rotation axis: 35/0/30
D574a
D567-3
116°
117°
118°
115°
31°
30°
0
50 km
N
Faults
Upper Cretaceous - Quaternary sediments
Lower Cretaceous red beds
Upper Jurassic - Lower Cretaceous volcanics
Middle Triassic - Middle Jurassic siliziclastics
Sinian - Lower Triassic sediments
Granitoids
Crystalline basement
Foziling/Luzhenguang greenschists/amphibolites
NW
Dabie
TLFZ
Qianshan Basin
Yangtze River depression
Jiangnan Uplift
SE
0
-5 km
-10 km
10 km
HP/UHP-Units
HP-Units
Cross-section: eastern Yangtze fold-thrust belt

Table 2
K/Ar and ^{40}Ar/^{39}Ar geochronology: sample descriptions and locations

Sample	Rock	N latitude	E longitude
A179	basalt granitic gneiss, Lushan massif granite in fold-thrust belt near Anqing	30°34′	116°52′
D277a	paragneiss, Dongling massif orthogneiss, Zhangbaling massif	29°29.82′	116°02.12′
D287b		30°37.36′	117°51.72′
D567d		30°34.37′	116°50.08′
D580		31°48.46′	117°38.06′

Sample	Mineral	%K	^{40}Ar (ng/g)	Age (Ma)
A179	whole rock	0.42 ± 0.15	4.15 ± 0.15	135 ± 5

Sample	Mineral	*J*	Weight (mg)	Grain size (μm)	Interpretation
D277a	ksp	0.0040588	1.5	400	rapid cooling at 96 ± 2 Ma, continuous cooling to 70 Ma rapid cooling at 120 ± 2 Ma
D287b	ksp	0.0040775	2.5	400	

Sample	Mineral	*J*	Weight (mg)	Grain size (μm)	TFA (Ma)	IA (Ma)	MSWD	^{40}Ar/ ^{36}Ar	WMA (Ma)	%^{39}Ar used
D567d	mus	0.00856	6.5	400	124.2 ± 1.4	126.9 ± 1.4	1.05/2.3	150 ± 68	124.8 ± 1.2	79
D580	bio	0.000788	6.2	400	103.4 ± 0.4	103.9 ± 0.7	57/1.7	293 ± 7	103.7 ± 0.3	96

J is the irradiation parameter; MSWD is the mean square weighted deviation (Wendt and Carl, 1991), which expresses the goodness of fit of the isochron (Roddick, 1978); isochron and weighted mean plateau ages are based on temperature steps underlain in gray in Fig. 7 and fraction of ^{39}Ar listed in the last column. ksp, potassium-feldspar; bio, biotite; mus, K-white mica.

Except for J66, the AFT ages of Triassic – Juras-Jurassic sediments from the eastern YFTB (J46, J57, J59, J78) range from 110 to 90 Ma. Only J57 (109.5 ± 5.9 Ma) was suitable for modeling. Its $T[t]$-path is not well constrained ($N=22$) with two different solutions, depending on the position of the initial constraints (Fig. 7c–b, c–c). The AFT and biotite ^{40}Ar/^{39}Ar ages of an orthogneiss from Zhangbaling (D580; 91.5 ±6.2, 103.7 ± 0.3 Ma, respectively; Table 2, Figs. 2 and 8) are also within the 110–90 Ma range.

Most (22) samples from the Dabie Shan and the YFTB have AFT ages in the range of 90–55 Ma, and eight samples have Eocene ages (45 ± 10 Ma; Fig. 2). The following discussion refers to those that were amenable to modeling and is based on the good-fit results (dark gray in Fig. 7). Y118 is from a granitoid along the southern edge of Dabie, close to a K_2–E red-bed basin. Its AFT age is 70.5 ± 2.9 Ma, and its confined track length distribution is skewed (mean 13 μm, $N=212$; Fig. 7f–a). Modeling with constraints that allow only continuous-cooling type $T[t]$-paths gives good-fit solutions if cooling started before 78 Ma (cooling rate: ~ 2 °C/Ma; Fig. 7f–b). The high initial temperature is due to the high thermal stability of the tracks ($D_{par}=3.5$ μm). Modeling was continued with an additional pair of central constraints. If the younger of these constraints is older than ~ 55 Ma, a broad envelope of good-fit $T[t]$ paths is obtained (Fig. 7f–c). Thus, even in a sample with a precisely determined AFT age and length distribution, the data are insufficient to impose severe restrictions on its thermal history. However, an envelope of $T[t]$-paths as in Fig. 7f–c must be interpreted as a superposition

Fig. 4. Mesoscopic fault data and map-scale structural interpretation of late Early Cretaceous stress field. NE–SW extension was accompanied by NW–SE shortening, which was mainly accomplished by folding and transpressive strike-slip faulting. Cross-section at the bottom is based on 1:200.000 geologic maps and own field investigations (R.G.S. Anhui, 1975). Pt: Proterozoic Yangtze basement; Z: Sinian; €: Cambrian; O: Ordovician, S: Silurian, D: Devonian; CP: Carboniferous–Permian; T: Early Triassic; T_2–J_2: mid-Triassic–mid-Jurassic; K_2–E: Late Cretaceous–Eocene.

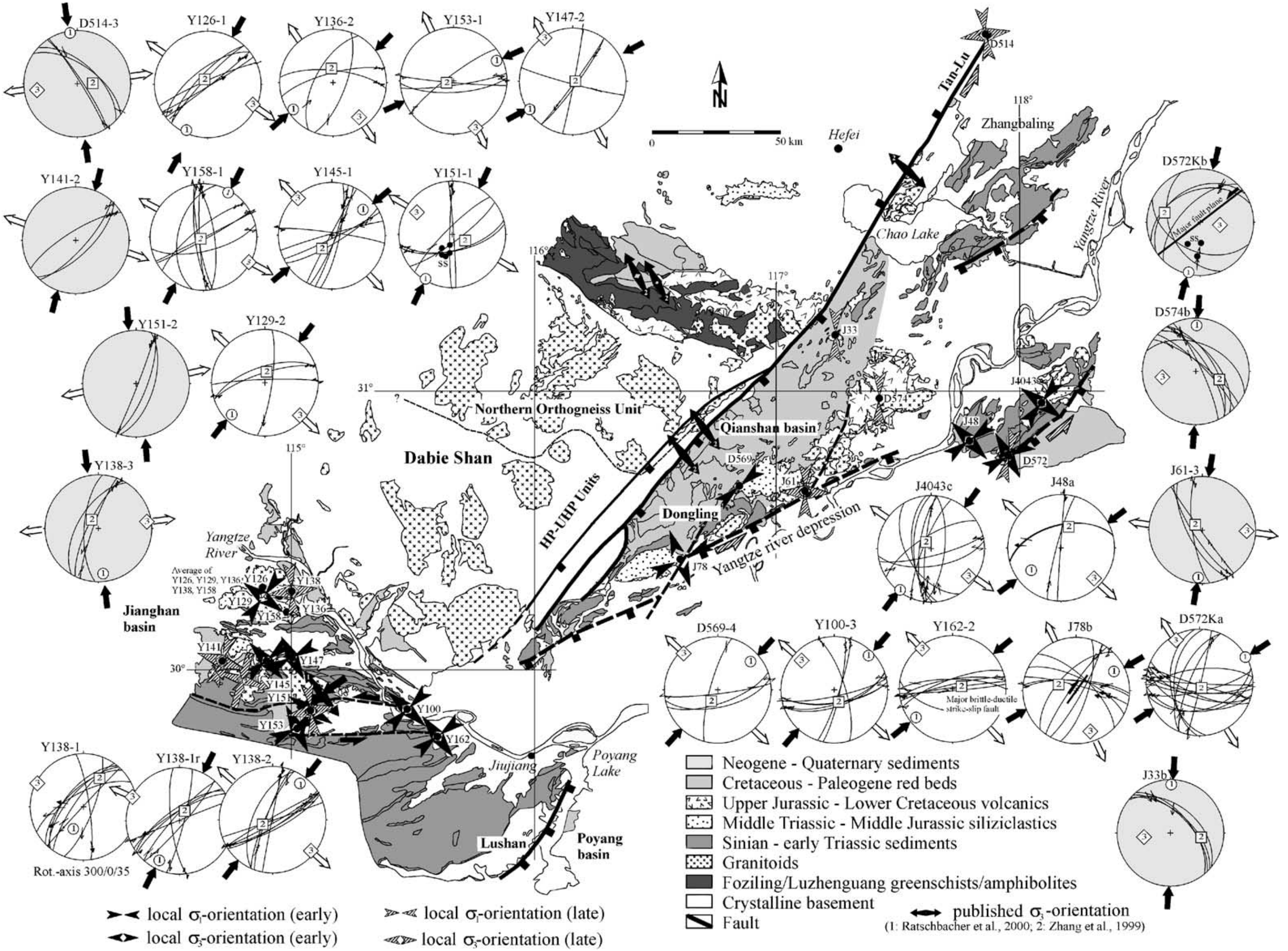

Fig. 5. Mesoscopic fault data and map-scale structural interpretation of Late Cretaceous–Paleogene stress fields. Faults active during NW–SE transtension (stress field 1 in text) are drawn on the map. Younger ~ N–S shortening was mainly accomplished by oblique thrusting (related stereograms are underlain gray); this sinistral reactivation of former normal faults is indicated by ruled arrows and σ_1 and σ_3 symbols in the map.

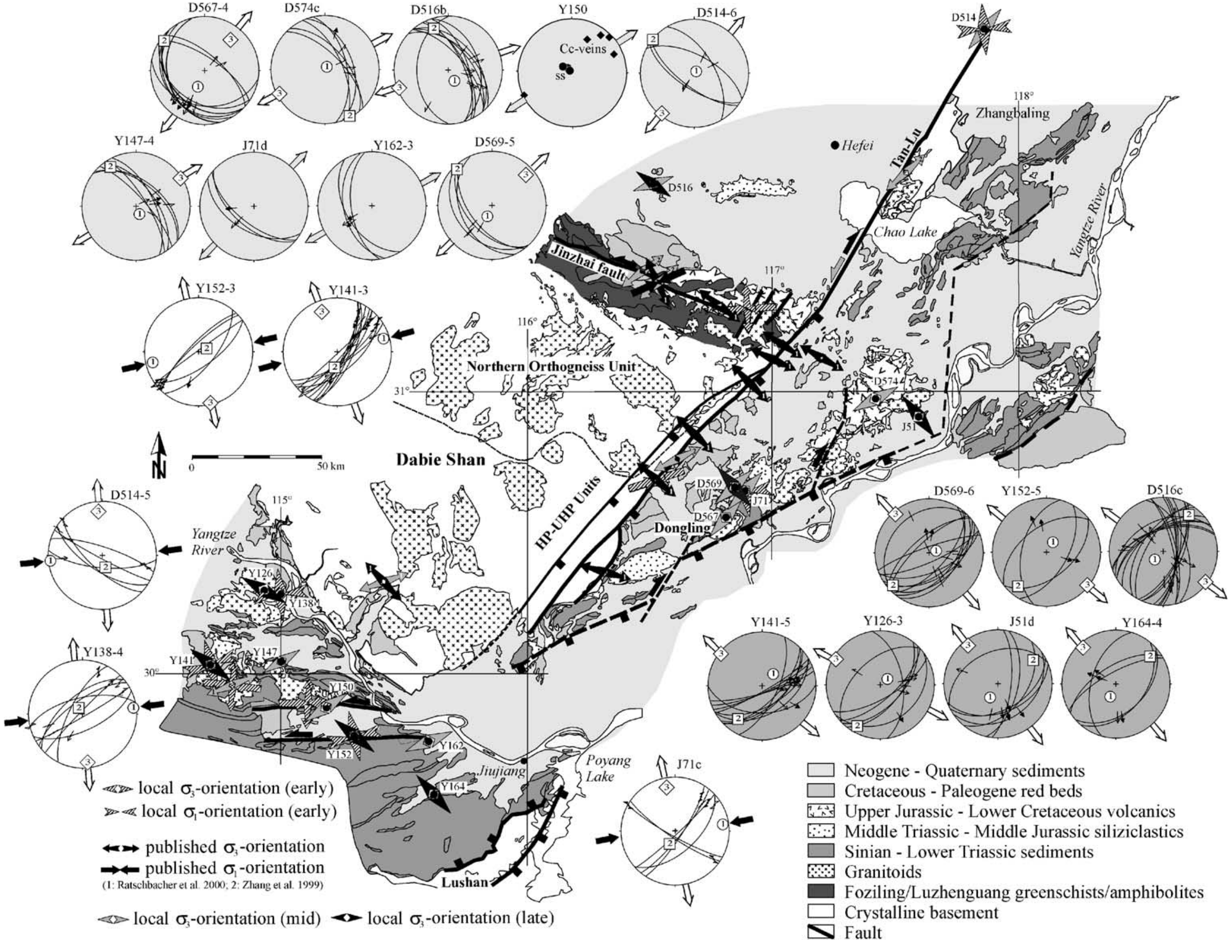

Fig. 6. Mesoscopic fault data and map-scale structural interpretation of late Cenozoic stress fields. The three fields are discriminated by different shading in the stereograms; the darker the underlay, the younger the related stress fields. Most faults in the map are reactivated Late Cretaceous – Paleogene faults. Ruled, gray, and black symbols on the map are related to early, intermediate, and late stress fields, respectively.

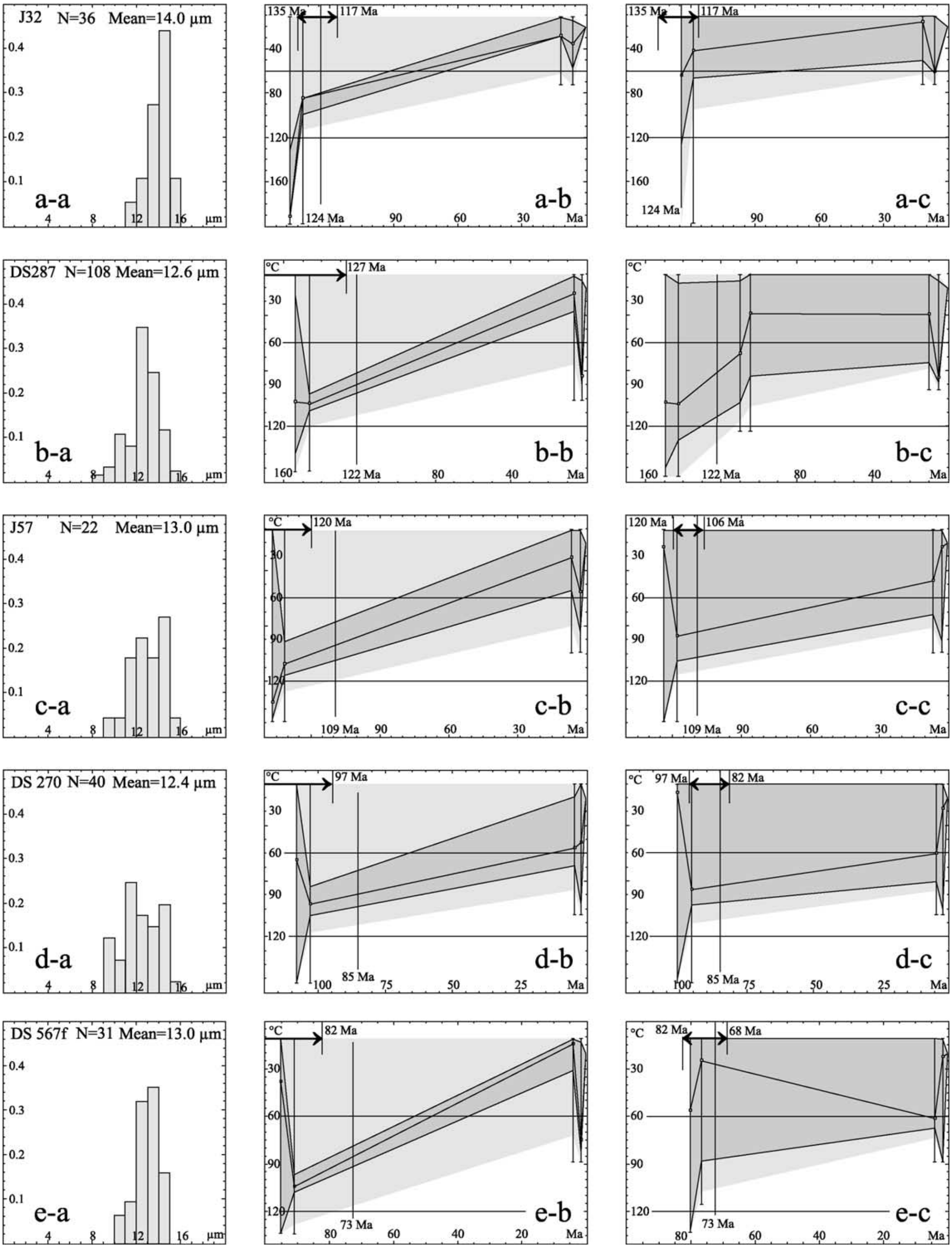
J32 N=36 Mean=14.0 µm
a-a
a-b
a-c
135 Ma
117 Ma
124 Ma
DS287 N=108 Mean=12.6 µm
b-a
b-b
b-c
127 Ma
122 Ma
J57 N=22 Mean=13.0 µm
c-a
c-b
c-c
120 Ma
106 Ma
109 Ma
DS 270 N=40 Mean=12.4 µm
d-a
d-b
d-c
97 Ma
82 Ma
85 Ma
DS 567f N=31 Mean=13.0 µm
e-a
e-b
e-c
82 Ma
68 Ma
73 Ma
°C
Ma
µm
0.1
0.2
0.3
0.4
4
8
12
16
30
60
90
120
160

Fig. 7.

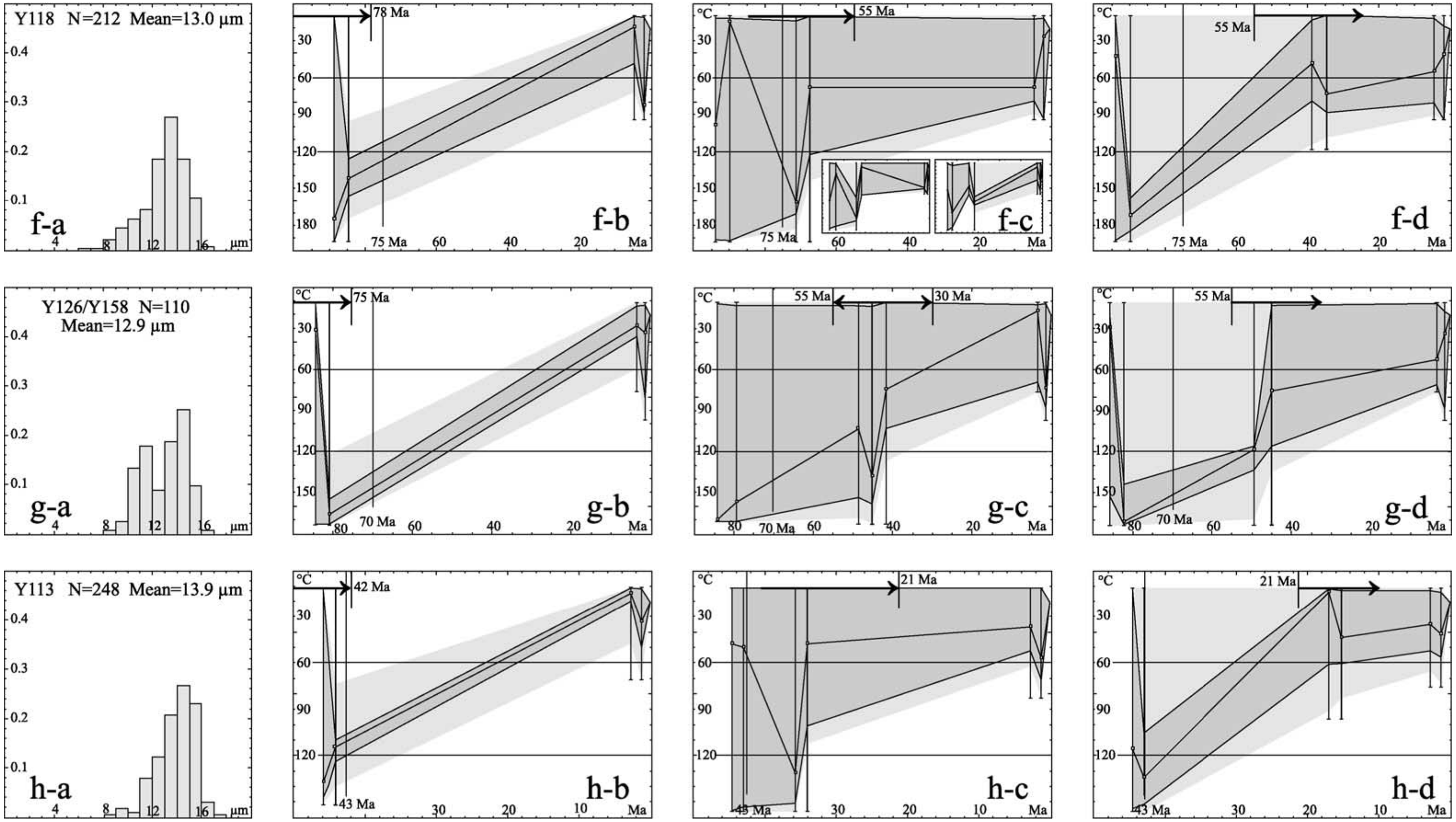

Fig. 7. Confined track-length distributions and range of $T[t]$-paths for the samples modeled with AFTSolve 1.1.3 (Ketcham et al., 2000). The arrows and ages at the top of each diagram indicate the range of constraints for which each particular type of $T[t]$-solution was obtained; this range refers to the constraint shown as a bold vertical line. The discussion refers only to the good-fit solutions (dark gray); the acceptable-fit solutions (light gray) are shown for reference. Horizontal lines represent the 60 and 120 °C isotherms. The vertical line and the value at the bottom of it represent the fission-track age calculated by AFTSolve from the single grain ages. In some cases, this age may deviate from the ages reported in Table 3, depending on whether the weighted or unweighted mean was adopted as the final age.

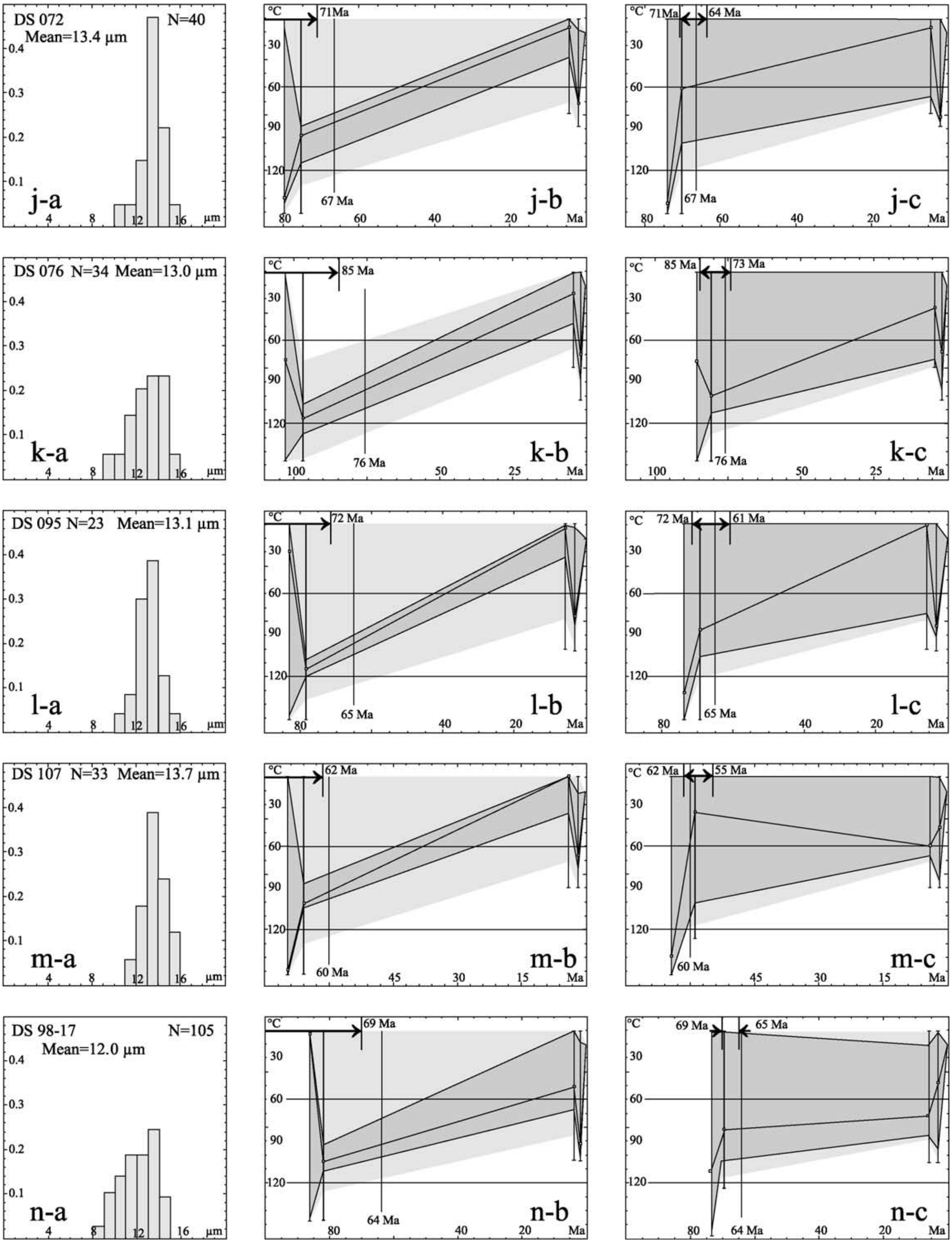

Fig. 7 (*continued*).

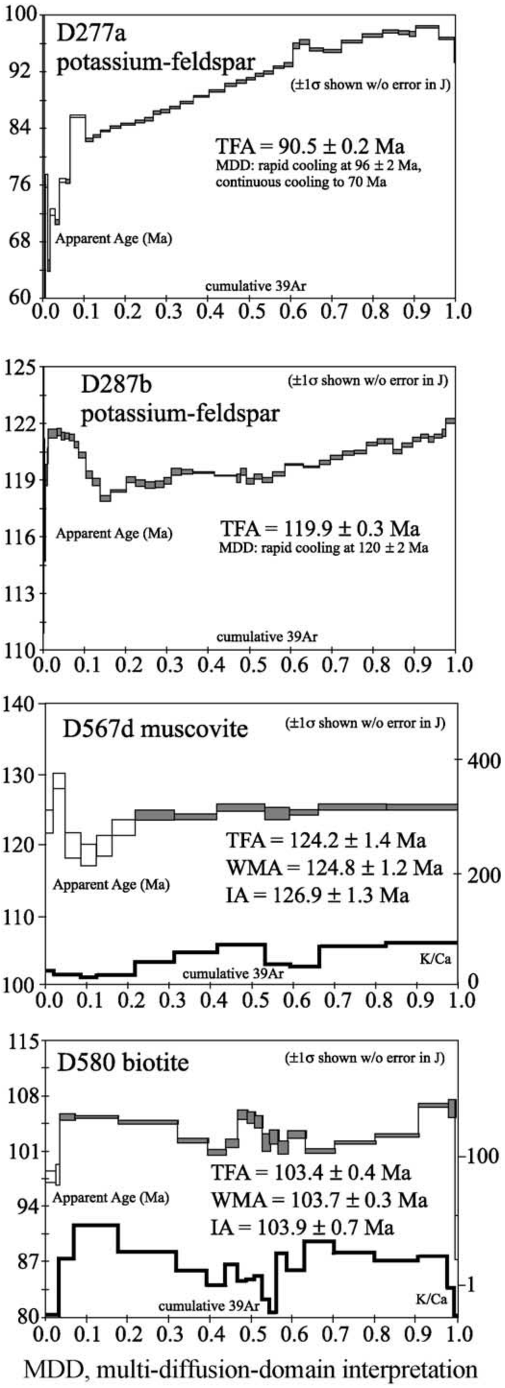

Fig. 8. New ^{40}Ar/^{39}Ar ages from the Yangtze foreland fold-thrust belt and the Zhangbaling area. See Table 2 for location and analytical data.

of different types of good-fit $T[t]$-paths (e.g. insets in Fig. 7f–c). There is no simple method to resolve the separate components; a good-fit solution was obtained when the younger of the pair of central constraints was set at < 55 Ma (Fig. 7f–d).

Samples Y126 (65.4 ± 1.8 Ma) and Y158 (64.1 ± 2.5 Ma) are Jurassic and Triassic sandstones from adjacent localities. Their similar ages and length distributions indicate that their AFT systems were reset after sedimentation, and that both samples experienced identical thermal histories. Their combined length distribution (mean 12.9 μm, $N = 110$) is bimodal (Fig. 7g–a), with the first maximum at ~ 11 μm somewhat less pronounced than the second at ~ 14 μm. The data were first modeled without central constraints, producing a narrow range of continuous-cooling type $T[t]$-paths (~ 1 °C/Ma), provided that effective track accumulation started no later than ~ 75 Ma (Fig. 7g–b). The data were also modeled with a triplet of central constraints that allows examining the range of solutions involving a thermal maximum. The result (Fig. 7g–c) must be interpreted as a superposition of different types of $T[t]$-path, including those corresponding to continuous cooling and a thermal event. Detailed modeling showed that 55–30 Ma brackets the thermal maximum (>150 °C; $D_{\mathrm{par}} = 4.0$ μm). However, the track-length distributions for those $T[t]$-paths showed that the length maxima are less clearly separated than in the measured length distribution. Modeling was repeated with only a pair of central constraints to explore simpler thermal histories involving changes in cooling rate. The resulting $T[t]$-paths (Fig. 7g–d) provide an equally good fit to the data and involve an initial phase of slow cooling (~ 1 °C/Ma) followed by a distinct phase of accelerated cooling, after which the temperature remained constant or decreased slowly.

Y113 is a biotite–garnet gneiss from the southern Dabie Shan with a fission-track age of 42.7 ± 1.6 Ma and a skewed length distribution (mean 13.9 μm, $N = 248$; Fig. 7h–a). Modeling with only initial and final constraints gives a narrow range of good-fit continuous-cooling type $T[t]$-paths, if the younger initial constraint is set at >42 Ma (Fig. 7h–b). Adding a pair of central constraints produces the same two solutions as for Y118: (1) a superposition of different types of $T[t]$ path, if the younger central constraint is set at >21 Ma (Fig. 7h–c), and (2) a well-defined $T[t]$-path with an initial phase of rapid cooling (3–5 °C/Ma), followed by slow cooling or constant temperature, if the younger central constraint is set at <21 Ma (Fig. 7h–d).

D270 is a granite from the southern YFTB that yielded an $^{40}Ar/^{39}Ar$ biotite age of 142.8 ± 2 Ma (Ratschbacher et al., 2000). Its AFT age is 85.4 ± 3.1 Ma, and its track-length distribution is broad and unimodal (mean 12.4 μm, $N=40$; Fig. 7d–a). Setting the initial constraints older than 97 Ma forces the $T[t]$-paths to pass through the closure temperature at the time given by the apparent AFT age, producing well-defined continuous cooling $T[t]$-solutions (Fig. 7d–b). With younger initial constraints (97–82 Ma), this condition is automatically satisfied, leading to $T[t]$-paths that are poorly constrained by the length distribution alone, and the best-fit solution indicates a long residence at the top of the PAZ (Fig. 7d–c).

D567f is from a granite in the Dongling basement dome. Its AFT age of 72.8 ± 3.9 Ma is interpreted as reflecting exhumation during the Late Cretaceous, an interpretation supported by the presence of K_2–E sediments in the hanging wall of the normal fault to the SE. Its length distribution is tight and unimodal (mean 13 μm, $N=31$; Fig. 7e–a). Modeling produces an envelope of good-fit $T[t]$-paths showing an initial phase of rapid cooling between 82 and 68 Ma, followed by a phase of slow cooling or constant temperature (Fig. 7e–c). Modeling with the younger initial constraint set at >82 Ma produces continuous-cooling type $T[t]$-paths that pass through the closure temperature at the time given by the AFT age (Fig. 7e–b).

Samples D76 (75.4 ± 2.9 Ma), D72 (67.2 ± 3.2 Ma), D95 (65.2 ± 2.8 Ma), D98-17 (60.2 ± 1.5 Ma), and D107 (57.6 ± 2.0 Ma) are granites and gneisses from the eastern and northern part of the Dabie basement. Their ages are also interpreted as reflecting differential exhumation during the Late Cretaceous and early Tertiary. Their track length distributions are unimodal with means between 12.0 and 13.7 μm. Few confined track lengths could be measured in most samples ($N=23–40$) except in D98-17 ($N=105$). In all cases, there are two types of solution. The first, involving continuous cooling at a moderate rate (1–2 °C/Ma), results from setting the initial constraints well above the apparent AFT age, forcing the $T[t]$-path to pass through the closure temperature at the time corresponding to this age (Fig. 7j–b, k–b, l–b, m–b, n–b). When the constraints are set at a lower age, the result is a broad envelope of $T[t]$-paths, involving an initial phase of rapid cooling followed by residence in the total stability zone and at the top of the PAZ (Fig. 7j–c, k–c, l–c, m–c, n–c).

4. Discussion

4.1. Early Cretaceous magmatism

With a few exceptions, the Dabie Shan and YFTB samples yielded Late Cretaceous to Paleogene AFT ages (Figs. 2 and 9) indicating that burial by sediments and/or regional metamorphism and magmatism reheated the Dabie basement and YFTB cover at the Jurassic stratigraphic to ≥ 100 °C level. Extensive Early Cretaceous plutonism, well dated at 137 to 125 Ma and concentrated within the Northern Orthogneiss Unit of northern Dabie, reheated the Dabie basement for the last time to >300 °C (Ratschbacher et al., 2000). Cretaceous volcanism and plutonism, less well dated from ~ 145 to 90 Ma, is widespread throughout eastern China (Fig. 9; e.g. Zheng, 1985; Lapierre et al., 1997). Regional cooling after the magmatism and related metamorphism is well documented by $^{40}Ar/^{39}Ar$ cooling ages within Dabie and the southern YFTB (Fig. 9; Ratschbacher et al., 2000). The AFT ages of intrusive rocks J32 and D287 extend the evidence for post-magmatic cooling to the eastern and northern foreland. Their $T[t]$-paths indicate rapid post-emplacement cooling to below ~ 100 °C at ~ 115 Ma after Early Cretaceous shallow emplacement, followed by residence in the total stability zone (Figs. 7 and 9). The AFT age of D516, the Lower Cretaceous sandstone from the northern Dabie foreland, implies the Dabie basement as its source area, with rapid cooling between 125 and 115 Ma in the source area, and subsequent rapid erosion, transport, and sedimentation. Together with the published $^{40}Ar/^{39}Ar$ ages (Hacker et al., 2000; Ratschbacher et al., 2000), this emphasizes the dominant role of Early Cretaceous exhumation in the northern Dabie Shan.

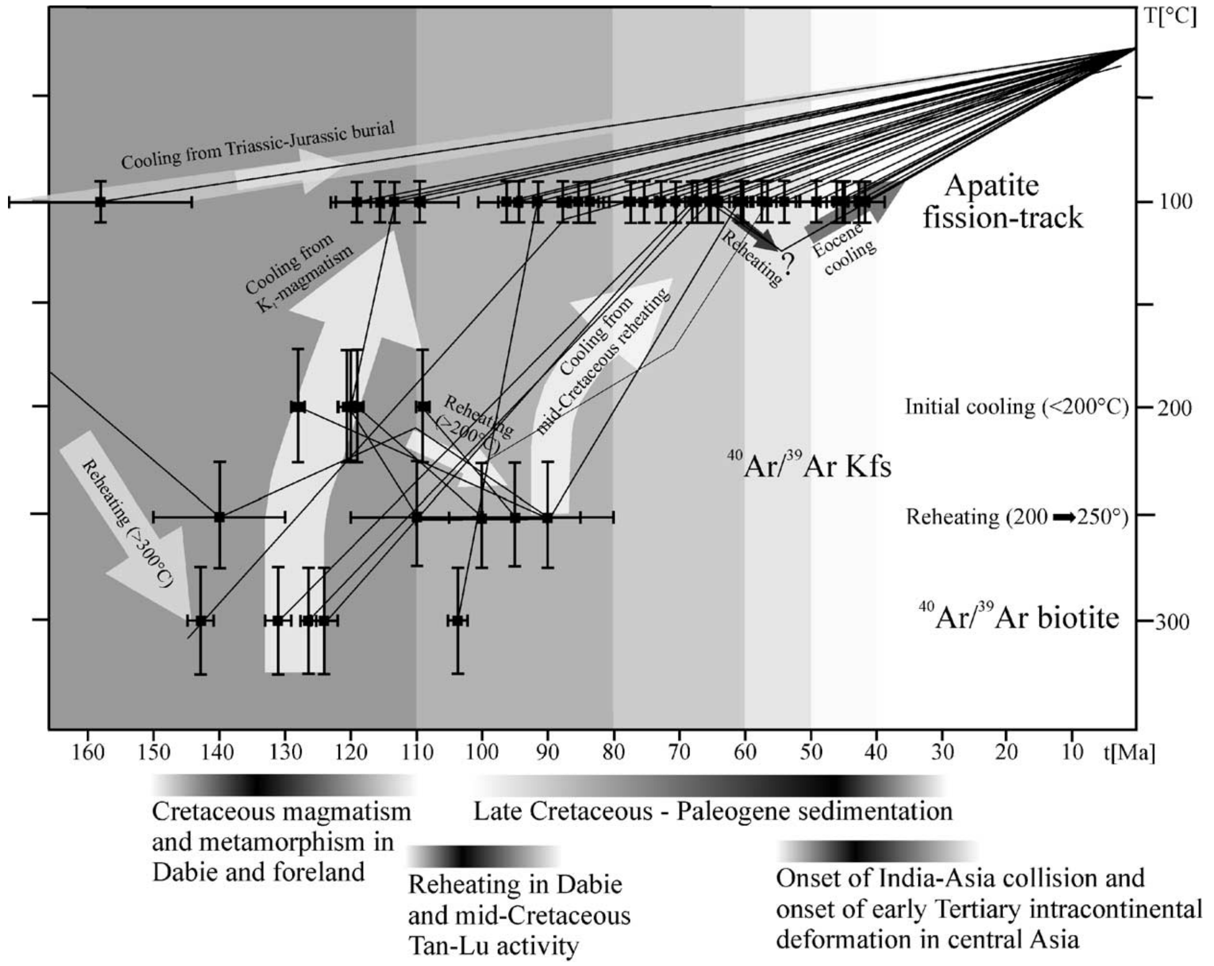

Fig. 9. Summary of tectonosedimentary and thermal events in eastern China derived from regional geology, apatite fission-track dating (ϕ-ages), and ^{40}Ar/^{39}Ar biotite and potassium-feldspar ages. Potassium-feldspar and biotite ages are from this study and Ratschbacher et al. (2000). Some samples seem to have escaped mid-Cretaceous reheating but this is likely an apparent effect, as no potassium-feldspar age data are available from these samples.

4.2. Syn-orogenic sediments

Triassic and Jurassic clastic sedimentary rocks of the YFTB yielded AFT ages of ~ 110–90 Ma. These ages, younger than their depositional ages, demonstrate that AFT dating cannot provide information on their provenance and thus do not constrain the Triassic–Jurassic exhumation of the UHP rocks of the Dabie orogen.

Two interpretations may account for the mid-Cretaceous ages (Fig. 9). Either the rocks were buried to ≥ 4 km, i.e. below the apatite PAZ, or reheating during the Early Cretaceous magmatism erased the tracks within the detrital grains. In the latter case, the thermal aureoles of the plutons must have heated the Middle Triassic to Upper Jurassic rocks regionally to >100 °C. Sample J66 supports the burial interpretation at least at this location; its ~ 158 Ma age predates the regional ~ 145 to 120 Ma magmatism within Dabie and the YFTB (Ratschbacher et al., 2000). The Middle Triassic through the Late Jurassic syn-orogenic unroofing of the Dabie Shan may have been accomplished burial (Hacker et al., 2000), as coarse clastic rocks testify to high deposition rates. The 110–90 Ma ages in the YFTB probably indicate continuous cooling from the Late Jurassic, reaching the PAZ in the mid-Cretaceous (cooling rates < 1 °C/Ma from J57).

4.3. Late Cretaceous–Paleogene rifting in eastern China

Most AFT ages from Dabie range from 90 to 55 Ma, and all postdate the 110–90 Ma reheating and cooling event in eastern Dabie (Fig. 2, inset top left; Fig. 9) revealed by ^{40}Ar/^{39}Ar potassium-feldspar thermochronology (Ratschbacher et al., 2000). The reheating–cooling event likely relates to the 110–90 Ma fault gouge dates from the northern TLFZ (Chen et al., 1989b) and our new ^{40}Ar/^{39}Ar biotite and AFT ages from Zhangbaling (D580a; Tables 2 and 3). AFT age contouring (Fig. 2) indicates the superposition of two cooling trends in Dabie and its forelands: (1) Isochrones of ~ 110 to 70 Ma gradient strike NW, sub-parallel to the XMF and the southern boundary of Dabie, indicating differential exhumation of the Dabie basement against its northern and southern forelands. This trend likely reflects faulting mainly along the XMF during the mid-Cretaceous. (2) The ~ 70 to ~ 40 Ma isochrons, the lowermost thermochronologic signal picked up by the AFT method, trend sub-parallel to the Tan-Lu, indicating Late Cretaceous–Tertiary faulting concentrated along the TLFZ.

We correlate the 100–70 Ma cooling trend with tectonic activity within NE–SW extension and NW–SE shortening, the late Early Cretaceous stress field established by structural analysis, and the 70–40 Ma cooling trend with activity within Late Cretaceous – Paleogene stress field 1 ((W)NW–(E)SE extension). The intermediate N trend and the cutting across the TLFZ of the isochrones in northeastern Dabie indicates that Late Cretaceous – Tertiary vertical displacement along the TLFZ diminishes northeastward, with a reversion of the hanging wall–footwall relationship in the Zhangbaling area (Figs. 2 and 5).

In Dabie and its foreland, the 100–70 Ma cooling trend and the late Early Cretaceous stress field are marked by dextral (transtensive) XMF and sinistral (transtensive) TLFZ activity; initiation of this deformation is constrained to ≤ 127 Ma. In southeastern China, sinistral shear along the NNE striking Changle-Nanao shear zone (sub-parallel to the TLFZ) and related folding were active from ~ 121 Ma (U/Pb zircon age of syn-tectonic granite; Tong and Tobisch, 1996) to 107 Ma (^{40}Ar/^{39}Ar biotite of syn-tectonic granite; Wang and Lu, 2000). ^{40}Ar/^{39}Ar biotite ages as young as 75 Ma are present in the Changle-Nanao shear zone, but their relations to faulting and folding are unclear (Tong and Tobisch, 1996). We place the Changle-Nanao shear zone and other faults sub-parallel to the Pacific margin in eastern Asia in the same kinematic group as the TLFZ of Dabie.

In the Qinling, NW–SE shortening and coeval NE–SW extension coincided with deposition of Late Cretaceous red beds in pull-apart basins along WNW striking dextral strike-slip fault zones that are sub-parallel to the XMF (Ratschbacher et al., submitted for publication). There, ^{40}Ar/^{39}Ar potassium-feldspar dating brackets Late Cretaceous faulting between 101 and 63 Ma. In Tongbai–Hong'an, between the Qinling and Dabie, reactivation of a NW striking shear belt occurred at ~ 75 Ma (^{40}Ar/^{39}Ar of pseudotachylite and biotite; Webb et al., 1999). We place the dextral fault zones along the Qinling–Tongbai–Hong'an belt in the same kinematic group as the dextral XMF in the Dabie Shan.

In Dabie and its foreland, the 70–40 Ma cooling trend and the Late Cretaceous – Paleogene stress field 1 mark normal TLFZ activity. In the Qianshan basin of the eastern YFTB, the red beds of the Xunnan formation were deposited during the Campanian – Maastrichtian, are thus younger than ~ 85 Ma, and are unfolded (R.G.S. Anhui, 1975, 1987). The Qianshan basin red beds therefore postdate late Early Cretaceous NW–SE contraction and mark the onset of normal faulting and basin formation along the southern TLFZ. In aggregate, the thermochronologic, structural, and stratigraphic information suggests that the switch from the late Early Cretaceous NE–SW extension and NW–SE shortening to NW–SE extension (corresponding to stress field 1) occurred at 75 ± 10 Ma. A geodynamic scenario for the Cretaceous NW–SE transpression in eastern China between ~ 125 and 75 Ma likely involved the collision of the "West Philippine Block–South China Sea Landmass" (Faure et al., 1989; Lapierre et al., 1997) with Asia, followed by Pacific back-arc extension (Ratschbacher et al., submitted for publication).

Several samples from Dabie yielded Eocene ages (~ 55 to 40 Ma; Fig. 9). $T[t]$-path modeling, specifically designed to emphasize variations in cooling rate, indicates enhanced cooling at 45 ± 10 Ma (Figs. 2, 7 and 9). This event is also identified in the sediments of the southern YFTB close to Dabie (Y126, Y158, Y118; Figs. 2 and 7). Eocene–Oligocene cooling in the central Dabie Shan was also demonstrated by (U–Th)–He dating with ages between 32 and 38 Ma (Reiners et al., 2001). The early Tertiary ages are interpreted in terms of tectonic reactivation of the TLFZ rather than long-term cooling from mid-Cretaceous reheating. Consistently, the youngest (i.e. Eocene) AFT ages occur just west of the TLFZ. During this deformation, the eastern Dabie basement was further exhumed in the footwall of the TLFZ, while coeval sedimentation occurred in the hanging wall (Qianshan basin). The Paleocene–Eocene red beds of the Qianshan basin east of Dabie dip 8–33° to the NW and reach up to 5 km thickness along the TLFZ (R.G.S. Anhui, 1975, 1987; Ratschbacher et al., 2000).

Several other half-graben structures formed in the YFTB, e.g. the depression of the present-day Yangtze river (Fig. 5). The final exhumation of the basement domes, e.g. Lushan and Dongling in the YFTB, probably took place during the latest Cretaceous–Eocene and was accomplished by normal faulting concentrated SE of the domes, with coeval sedimentation of K_2–E red beds in the hanging wall. AFT thermochronology is unable to pick up the thermal signal of the Eocene exhumation as the rocks reached < 4 km during Late Cretaceous.

We are currently not able to define distinct stress fields for the Late Cretaceous and early Tertiary. Indeed, the stress fields in the Late Cretaceous and Paleogene seem to have had similar orientations (they may have rotated counterclockwise during late Paleogene, see stress fields 1 and 2). Our data suggest that the TLFZ was a normal fault during most of the latest Cretaceous–Paleogene and became sinistral transpressive at the end of this period (Fig. 3).

Formation of Paleocene to Eocene rift basins has been documented throughout eastern China (Fig. 1; e.g. Allen et al., 1997), where onshore Cenozoic basins cover an area of >500.000 km^2. The onset of normal faulting in the Weihe graben is dated at ~ 52 to 45 Ma (Zhang et al., 1999). In the North Jiangsu basin (Fig. 1), normal faulting triggered deposition of up to 9 km of Paleocene to Pliocene sediments (Zhou et al., 2000; Zhang et al., 1989). In the Bohai basin (Fig. 1), early syn-rift sediments were deposited at ~ 55 Ma during N(W)–S(E) dextral transtension (Allen et al., 1997). On one hand, rift-basin formation during the Mesozoic–Cenozoic in eastern China is generally attributed to intra-arc and/or back-arc rifting along the Pacific–Eurasian plate margin (e.g. Chen and Dickinson, 1986). Northrup et al. (1995) suggested a dynamic link between Pacific–Eurasia convergence and extension along the Eurasian margin by showing that the timing of extension along the east Eurasian plate boundary correlates with periods of reduced convergence between the Pacific or Philippine plate and Eurasia. The convergence rate decreased during early Tertiary and reached a minimum in the Eocene. Decreased convergence rates may have reduced plate coupling, which resulted in widespread extension along the eastern margin of Eurasia. On the other hand, Eocene NE–SW shortening across central Asia (e.g. Tibet, Tien Shan, Qilian Shan), and strike-slip and extensional faulting across northeastern Asia (e.g. Baikal rift, Shanxi rifts surrounding the Ordos block; Haiyuan, Kunlun, Gansu, and Qinling–Dabie strike-slip faults) are generally attributed to the India–Asia collision (e.g. Tapponnier and Molnar, 1977). Suturing along the Indus-Yarlong suture occurred at ~ 55 Ma (e.g. Searle et al., 1997; Makovsky et al., 1999), and Roger et al. (2000) suggested that intracontinental subduction in central Tibet started at ~ 50 Ma. A common argument against an impact of the India–Asia collision on extension in eastern China is the 1500–3000 km distance from the Indus-Yarlung suture (e.g. Allen et al., 1997; Northrup et al., 1995). However, it is also difficult to understand why the Weihe graben should have formed as a result of back-arc extension, as it is ~ 1500 km away from the active eastern Pacific margin (Fig. 1). Considering that no clear breaks in the orientation and the onset of extension in Cenozoic rifts in eastern Asia (e.g. Shanxi rifts and Qianshan basin) have been documented, the early Cenozoic tectono-sedimentary evolution of eastern China may be best interpreted as a result of combined effects of Pacific subduction and India–Asia collision (Fig. 9). We thus speculate that the 45 ± 10 Ma event in Dabie and the YFTB may provide the first age constraint on the initiation of far-field effects of the India–Asia collision in eastern China.

4.4. Late Cenozoic inversion and thermal subsidence

Regional late Oligocene inversion associated with a regional unconformity (~ 25 Ma) at the base of Neogene strata is documented from the East China Sea, and the Jianghan, Hehuai, Jiangsu, Bohai, and Songliao basins (Wang et al., 2000; Liu et al., 2000; Chen et al., 1989a; Hu et al., 1989; Ma et al., 1989; Allen et al., 1997). Allen et al. (1997) documented inversion of the Bohai Basin edges by dextral transpression. Stress field 3, the E–W shortening, portrays this inversion in Dabie and its foreland. The geodynamic cause of this regional inversion is poorly known. Allen et al. (1997) preferred an interpretation comprising a reorganization of oceanic plates along the Pacific margin due to collision of the Australian and the Philippine plates over mid-Tertiary reorganization of the India–Asia collision zone.

Neogene thermal subsidence in the rift basins was accompanied by only minor normal faulting lasting until today (e.g. Allen et al., 1997; Gilder et al., 1991). The Neogene stress field changed from early NE–SW to active (S)SE–(N)NW extension and the TLFZ thus changed from sinistral transtension via normal to present-day dextral transtension.

5. Conclusions

(1) Our new apatite fission-track (AFT) and structural data provide first tectonothermal constraints on the southern Tan-Lu fault zone (TLFZ), one of Asia's major faults, the late-stage exhumation history of the Dabie Shan, Earth's largest track of ultrahigh-pressure (UHP) exposure, and the Yangtze foreland fold-thrust belt (YFTB).

(2) The fission-track analyses compared the Durango, Fish Canyon, and Mt. Dromedary apatite age standards and utilized the independent (ϕ-), and the indirect Z- and ξ-methods for age determination. Mt. Dromedary apatite is not a useful standard, as its independent AFT age is ~ 20% lower than its reference age. After the exclusion of Mt. Dromedary, all three methods yielded statistically indistinguishable ages.

(3) Little significance can be attached to a single apatite temperature–time path. The range of possible $T[t]$-paths can be explored by repeated modeling of the same sample with systematic variation of the user-entered constraints, but more sophisticated software should be developed in due course.

(4) Our AFT ages of intrusive rocks extend the evidence for Early Cretaceous cooling in eastern China to the eastern and northern forelands of the Dabie Shan. The $T[t]$-paths indicate rapid post-emplacement cooling to below ~ 100 °C at ~ 115 Ma.

(5) Triassic and Jurassic clastic sedimentary rocks of the eastern YFTB yielded AFT ages of ~ 110 to 90 Ma. These ages, younger than the depositional ages, demonstrate that AFT dating cannot provide information on provenance and thus do not constrain the Triassic–Jurassic exhumation of the UHP rocks of the Dabie orogen.

(6) Isochrones of ~ 110 to 70 Ma cooling gradient strike NW, indicating differential exhumation of the Dabie basement against its northern and southern forelands. This trend and the associated late Early Cretaceous stress field marked normal (dextral transtensive) and sinistral (transtensive) activity along the Xiaotian–Mozitang fault of northern Dabie and the TLFZ of eastern Dabie, respectively. Isochrones of 70–40 Ma cooling gradient strike NE. The associated Late Cretaceous – Paleogene NW–SE extension in Dabie and its foreland indicates normal TLFZ activity and onset of basin formation (Qianshan basin). The thermochronologic, structural, and stratigraphic information suggests that the switch from the previous NE–SW extension to the NW–SE extension occurred at 75 ± 10 Ma. During the Late Cretaceous and early Tertiary several other extensional structures formed in the YFTB, e.g. the depression of the present-day Yangtze river, and final exhumation of the basement domes in the YFTB, e.g. Lushan and Dongling, took place. A geodynamic scenario for the Cretaceous – early Tertiary tectonics in eastern China involves the collision of the "West Philippine Block–South China Sea Landmass" with Asia, followed by Pacific back-arc extension.

(7) Several samples from Dabie yielded Eocene ages, and $T[t]$-path modeling indicates enhanced cooling at 45 ± 10 Ma. These early Tertiary ages are interpreted in terms of tectonic reactivation of the TLFZ, during which the eastern Dabie basement was further exhumed, while coeval sedimentation occurred in the hanging wall (Qianshan basin). This 45 ± 10 Ma event in Dabie and the YFTB may provide the

first age constraint on the initiation of far-field effects of the India–Asia collision in eastern China.

(8) Regional late Oligocene inversion associated with a regional unconformity (~ 25 Ma) at the base of Neogene strata is documented by E–W shortening in Dabie and its foreland. During the Neogene, the TLFZ changed from sinistral transtensional via normal to present-day dextral transtensional motion.

Acknowledgements

Zhang Yueqiao is thanked for numerous discussions and excellent field guidance. LR and BRH thank Mike McWilliams for access to his Ar/Ar laboratory at Stanford. Wolfgang Frank (Vienna) provided the dating of sample D567d and Yury Pushkarev (St. Petersburg) that of sample A179. Ray Donelick made the Cf irradiations possible. Denis Gapais and an anonymous reviewer are thanked for constructive comments. The Deutsche Forschungsgemeinschaft (grants Ra442/14, 19; Wa287/13) funded field and laboratory work.

Appendix A. Fault-slip analysis

Fault slip data were collected from outcrops of known or assumed stratigraphic position. Each station is an outcrop of up to quarry size with uniform lithology. Sense of slip along the faults was deduced from kinematic indicators, e.g. offset markers, fibrous minerals grown behind fault steps, Riedel shears, tension gashes, and slickenlines (e.g. Petit et al., 1983). Because errors in slip sense determination may have severe effects on the calculation of principal stress axes, a confidence level was assigned to each slip sense datum. These levels are recorded in the style of the arrowheads expressing the slip direction of the hanging wall block in the fault slip data diagrams, thus allowing judgment of the quality of the database. Surface morphology of the slickensides and fault size, classified qualitatively by estimating the displacement and the lateral extent of the fault were recorded. The aim was to identify first-order faults and to enable a comparison of faults measured in outcrops with those inferred from mapping. Indications of multiple slip were recorded, and the relative chronology was used for separation of heterogeneous raw data fault sets into subsets. Overprinting relationships such as consistent fault superposition, overgrowths of differently oriented fibers, or fibers with changing growth direction guided the assignment of the subsets to relative age groups. In order to achieve a regionally consistent age relationship, comparisons of outcrops of different stratigraphic ages are necessary. We preferred outcrops with weak deformation and which allow assessing relations between folding and faulting. We mostly stayed away from large-scale faults, as they potentially cause stress perturbations and thus provide little information about the regional stress field.

We used the computer program package of Sperner et al. (1993) for fault-slip analysis to calculate the orientation of principal stress axes and the reduced stress tensors (e.g. Angelier, 1984). Out of this package, we obtained stress axes by the "pressure–tension (P–B–T) axes" method (Turner, 1953) and calculated stress tensors by the "numerical dynamic analysis" of Spang (1972). In addition to stress orientation, the computation of the reduced stress tensor determines the ratio R, which expresses the relationship between the magnitudes of the principal stresses. Extreme values of R correspond to stress ellipsoids with $\sigma_2 = \sigma_3$ ($R = 0$) or $\sigma_1 = \sigma_2$ ($R = 1$). The quality and the quantity of field data determined the selection of the method used for calculation. The P–B–T axes method was used with scarce data and where insufficient time was available in the field for careful analysis of fault and striae characteristics.

Appendix B. Apatite fission-track analysis

B.1. Sample preparation, irradiation, age calculation, and standards

The apatite fractions were separated using heavy-liquid and electromagnetic techniques, mounted in epoxy, ground, and polished. The mounts were etched for 70 s in 2.5% HNO_3 at room temperature, covered with 50 μm muscovite external detectors and irradiated in channels 7 (epithermal/thermal fluence ratio: $f = 116$; epithermal neutron spectrum: $\varphi_e(E) \sim 1/E^{(1+\alpha)}$ ($\alpha = 0.072$; De Corte et al., 1986), 8 ($f = 163$; $\alpha = 0.068$), and 15 ($f = 68.5$; $\alpha = 0.065$) of the Thetis reactor at the Institute for Nuclear Sciences in Gent.

Table 3
Apatite fission-track data, rock description and sample locations

Sample	Lithology	Latitude N	Longitude E	Grains	N_s	N_i	ρ_D (10^6 cm^{-2})	ϕ (10^{15} cm^{-2})	Z (10^8 year)	ζ (year cm^2)	P (χ^2)	ϕ-age (Ma)	ζ-age (Ma)	Z-age (Ma)
DS 012[a]	Gneiss	30°27.500′	116°18.200′	18	165	1167				320	0.940		49.3 ± 4.1	
DS 025	Gneiss	31°18.300′	115°56.900′	7	89	334	1.63	9.64	5.74	369	0.156	77.4 ± 9.4	79.7 ± 9.7	76.0 ± 9.3
DS 043	Grt-Bt-schist	31°22.400′	116°11.500′	27	276	917	1.64	9.67	5.76	369	0.205	87.7 ± 6.3	90.2 ± 6.5	86.0 ± 6.4
DS 058	Hbl-Bt-gabbro	31°14.340′	116°20.390′	20	1912	6671	1.64	9.73	5.78	369	0.021	83.6 ± 3.0	85.8 ± 3.1	81.9 ± 3.0
DS 072	Gneiss	31°07.480′	116°31.520′	26	664	2885	1.65	9.67	5.79	369	0.266	67.2 ± 3.2	69.6 ± 3.4	66.3 ± 3.4
DS 076	Granite	30°47.000′	116°05.000′	20	1116	4383	1.66	9.82	5.82	369	0.392	75.4 ± 2.9	77.3 ± 3.1	73.6 ± 3.2
DS 095	UHP-gneiss	30°42.470′	116°23.260′	25	881	4014	1.66	9.84	5.83	369	0.509	65.2 ± 2.8	66.3 ± 2.9	63.7 ± 3.0
DS 099	UHP-gneiss	30°40.000′	116°27.000′	20	812	4125	1.66	9.87	5.84	369	0.000	54.0 ± 2.4	55.4 ± 2.3	52.7 ± 2.2
DS 103	UHP-gneiss	30°40.000′	116°27.000′	22	1041	3485	1.57	9.90	5.17	341	0.000	68.1 ± 2.6	70.8 ± 2.6	68.6 ± 2.6
DS 107	UHP-gneiss	30°32.480′	116°17.010′	25	1197	5994	1.67	9.93	5.87	369	0.037	57.6 ± 2.0	58.9 ± 1.9	56.0 ± 1.8
DS 123	Gneiss	30°24.530′	116°07.200′	6	43	140	1.68	9.99	5.89	369	0.020	60.6 ± 13.1	62.1 ± 13.2	59.1 ± 12.6
DS 270	Granite	29°59.910′	114°50.250′	15	1435	4288	1.57	10.1	5.17	341	0.370	85.4 ± 3.1	88.7 ± 3.1	85.9 ± 2.6
DS 277	Granite	29°30.810′	116°02.360′	42	772	3479	1.57	10.1	5.17	341	0.120	56.8 ± 2.5	59.0 ± 2.6	57.1 ± 2.3
DS 287	Diorite	30°37.360′	116°51.720′	25	1977	4946	1.71	10.2	5.89	369	0.000	113.3 ± 3.6	115.6 ± 3.3	109.5 ± 3.1
DS 516	K_1 sandstone	31°43.140′	116°30.584′	14	954	714	0.387	2.58	1.53	369	0.034	115.5 ± 6.7	105.4 ± 6.1	112.9 ± 6.5
DS 543	Quartzite	31°27.736′	116°10.498′	40	3204	3337	0.387	2.51	1.53	369	0.129	72.7 ± 2.3	68.2 ± 2.4	73.0 ± 3.3
DS 545	Qz-Bt gneiss	31°28.975′	116°12.173′	7	343	402	0.387	2.49	1.53	369	0.782	64.1 ± 4.9	60.6 ± 4.7	64.9 ± 5.4
DS 554a	Granite	30°50.527′	116°17.598′	12	219	397	0.650	4.02	0.220	341	0.850	56.6 ± 4.9	60.8 ± 5.2	60.5 ± 5.1
DS 555	Granite	30°48.985′	116°15.476′	16	1233	2009	0.650	4.02	0.220	341	0.001	57.4 ± 2.2	61.7 ± 2.3	61.1 ± 2.3
DS 559	UHP-gneiss	30°40.040′	116°29.041′	17	370	825	0.650	4.02	0.220	341	0.450	46.1 ± 3.0	49.5 ± 3.2	49.2 ± 3.3
DS 561	Gneiss	30°27.794′	116°14.837′	12	281	640	0.650	4.02	0.220	341	0.520	45.1 ± 3.4	48.5 ± 3.5	48.2 ± 3.5
DS 565a	Gneiss	30°27.225′	116°16.488′	26	1127	2394	0.650	4.02	0.220	341	0.010	44.8 ± 1.7	48.1 ± 1.8	47.7 ± 1.8
DS 567f	Granite	30°33.236′	116°49.800′	22	534	1549		8.26			0.443	72.8 ± 3.9		
DS 580	Gneiss	31°49.700′	117°38.700′	19	340	783		8.26			0.998	91.5 ± 6.2		
J 32	Subvolcanic	31°19.400′	117°11.900′	21	1747	2969		8.26			0.007	117.8 ± 3.7		
J 46	T_2 sandstone	30°55.200′	117°54.500′	38	1171	882	0.490	3.25	1.63	341	0.030	102.0 ± 3.6	103.0 ± 3.6	99.7 ± 3.5
J 57	J_1/J_2 sandstone	30°49.800′	117°16.400′	15	600	1153		8.26			0.546	109.5 ± 5.9		
J 59	J_2/J_3 sandstone	30°49.600′	117°16.300′	20	982	2145		8.26			0.219	96.4 ± 4.2		
J 66	T_2 sandstone	30°39.900′	116°59.300′	6	225	298		8.26			0.804	158.2 ± 14.3		
J 78	J_2 sandstone	30°24.300′	116°36.500′	7	355	792		8.26			0.502	94.4 ± 6.3		
DS 91-28[a]	Gneiss	30°45.500′	115°44.400′	20	144	569				320	0.980		80.2 ± 7.5	
DS 91-34[a]	Gneiss	30°48.400′	115°49.000′	20	132	605				320	0.860		68.4 ± 6.6	
DS 91-64[a]	Gneiss	30°45.700′	115°46.700′	20	76	337				320	0.990		70.7 ± 9.0	
DS 98-17	Gneiss	31°10.299′	116°32.279′	34	4271	4844	0.387	2.41	1.53	369	0.000	60.2 ± 1.5	59.0 ± 1.3	63.1 ± 1.4
DS 98-33	UHP-gneiss	30°47.861′	116°15.223′	16	413	2199	1.74	10.4	6.05	369	0.000	49.1 ± 3.1	50.8 ± 3.0	47.9 ± 2.8
DS 98-35	UHP-gneiss	30°46.827′	116°13.681′	11	435	2339	1.74	10.4	6.06	369	0.000	41.7 ± 3.0	46.2 ± 2.8	43.3 ± 2.7
Y 113	Gneiss	30°27.010′	115°47.209′	16	1389	2709	4.70	3.25	1.63	341	0.800	42.7 ± 1.6	40.9 ± 1.5	41.7 ± 1.4
Y 118	Granite	30°18.310′	115°09.400′	15	1235	1356	4.70	3.25	1.63	341	0.020	70.5 ± 2.9	67.6 ± 2.7	68.9 ± 2.8
Y 126	J_2 sandstone	30°18.225′	114°57.130′	47	2671	3159	4.90	3.25	1.63	341	0.002	65.4 ± 1.8	66.3 ± 1.8	63.9 ± 1.7
Y 158	T_2 sandstone	30°14.571′	115°00.978′	47	1338	1521	5.00	3.25	1.63	341	0.004	64.1 ± 2.5	66.7 ± 2.6	62.6 ± 2.5

N_s: number of spontaneous tracks, N_i: number of induced tracks, ρ_D: track density in standard uranium glass, ϕ: thermal neutron fluence, ζ: ζ-calibration factor, Z: Z-calibration factor. T_2: Middle Triassic, J_1: Early Jurassic, J_2: Middle Jurassic, J_3: Late Jurassic, K_1: Early Cretaceous, K_2–E: Late Cretaceous–Eocene, Qz: quartz, Bt: biotite, Grt: garnet, Hbl: hornblende, UHP: ultrahigh-pressure.

[a] Determined by Ann Blythe ($\zeta_{SRM962a} = 320 \pm 9$ year cm^2).

The muscovite external detectors were etched in 40% HF for 20 min at room temperature.

The thermal neutron fluence was calculated from the 411.8 keV gamma-activity of Al–0.1%Au neutron fluence monitors (IRMM 530R), inserted at the top, middle, and bottom of the irradiation cans, and measured at the reference height of a Ge(Li) detector connected to a Canberra 4000 channel gamma-spectrometer. Reactor staff with the aid of primary and secondary standard sources determined the peak detection efficiency at this height. Counting was continued till the Poisson uncertainty on the peak area amounted to $<0.5\%$. The thermal neutron fluences were calculated in the Høgdahl convention, using the following constants: atomic mass, $M_{\mathrm{Au}}=196.97$ (Holden, 1995); isotopic abundance of ^{197}Au, $^{197}\theta=1$ (Holden, 1995); 2200 m/s effective cross-section for the ^{197}Au(n,γ)-reaction, $\sigma_0=98.65$ b (Mughabghab et al., 1981; Holden and Holden, 1989); resonance energy, $E_{\mathrm{r}}=5.65$ eV (Jovanović et al., 1987); resonance integral, $I_0=1550$ b (Mughabghab et al., 1981); decay constant for $^{198}\mathrm{Au}\rightarrow{}^{198}\mathrm{Hg}+\beta^{-}+\gamma$ (411.8 keV), $\lambda=2.97663\ 10^{-6}\ \mathrm{s}^{-1}$ (Hoppes and Schima, 1982); gamma intensity, $I_{411.8\ \mathrm{keV}}=0.9556$ (Hoppes and Schima, 1982). The thermal neutron fluences are summarized in Table 3; their combined systematic and statistical error is estimated at ~ 2% (Van den haute et al., 1988; Jonckheere, 1995).

To check the accuracy of the age determinations with the independent method (ϕ-method), a set of samples was also dated with the Z- and ζ-methods. Two mounts of the Fish Canyon tuff, Durango, and Mt. Dromedary age standards were included in each irradiation. These were prepared in the same manner as the samples, with two exceptions (Jonckheere and Wagner, 2000). First, ~ 1-mm-thick slices, cut parallel to the prismatic faces of a single crystal of Durango apatite, were used instead of shards obtained by crushing. This ensures that the track counts in the age standard are performed on the same surfaces that are selected for the AFT counts in the samples. Second, mm-sized shards of the Corning CN5 standard uranium glass were embedded together with the age standards. This ensures a minimum separation between the standard glasses and apatite age standards.

An analysis of the ζ-calibration factors demonstrated a systematic difference between those for the Fish Canyon tuff and Durango apatite and that for the Mount Dromedary apatite. The independent ages of the Fish Canyon tuff and Durango apatites are in agreement with their reference ages, whereas that of the Mt. Dromedary apatite is ~ 20% too low (see also Jonckheere et al., 2000). We concluded that the reference age of the Mt. Dromedary apatite is not reliable, and calculated the Z- and ξ-calibration factors on the basis of the results for the Fish Canyon tuff and Durango apatites alone. The unweighted rather than the weighted mean was used, because the latter tends to be biased in favor of lower values; the error on the unweighted mean ξ also reflects the true scatter of the data. The ξ-values in Table 3 show that there exists a significant difference between the mean ξ-values for the two principal analysts ($\xi_{\mathrm{CN5}}=341\pm4$ year cm^2 and $\xi_{\mathrm{CN5}}=369\pm7$ year cm^2), which is ascribed to different track identification criteria. However, both analysts obtained ξ-ages for all samples that are in agreement with their independent fission-track ages (ϕ-ages) and Z-ages (Fig. A1). It is thus safe to conclude that their different track identification criteria did not introduce systematic errors.

The independent fission-track ages were calculated using the equation:

$$t = 1/\lambda_{\alpha}\ln[(\lambda_{\alpha}/\lambda_{\mathrm{f}})\mathrm{GR}(\rho_{\mathrm{s}}/\rho_{\mathrm{i}})I\phi_{\mathrm{s}}\sigma_0+1],$$

wherein the nuclear parameters take the following values: alpha-decay constant of ^{238}U, $\lambda_{\alpha}=1.551\times10^{-10}$ year^{-1} (Jaffey et al., 1971); fission-decay constant of ^{238}U, $\lambda_{\mathrm{f}}=8.46\times10^{-17}$ year^{-1} (Galliker et al., 1970; Guedes et al., 2000); geometry factor, $G=0.5$; isotopic ratio $^{235}\mathrm{U}/^{238}\mathrm{U}$, $I=7.253\times10^{-3}$ (Cowan and Adler, 1976); ϕ_{s}, subcadmium neutron fluence in the Høgdahl convention; effective 2200 m/s cross-section for the ^{235}U(n,f)-reaction, $\sigma_0=586$ b (Holden and Holden, 1989). The R-factor represents the ratio of the track counting efficiencies in an apatite internal surface and a muscovite external detector. R depends on the track identification criteria, and is a personal calibration factor in the same way as ζ. R was determined from the ratio of induced track densities in internal apatite surfaces and co-irradiated external detectors (Jonckheere, 1995) and from the ratio of the reference ages of a set of age standards to their ϕ-ages (Enkelmann, 2001). The R-values of the two principal analysts ($R=1.03\pm0.01$ and $R=1.20\pm$

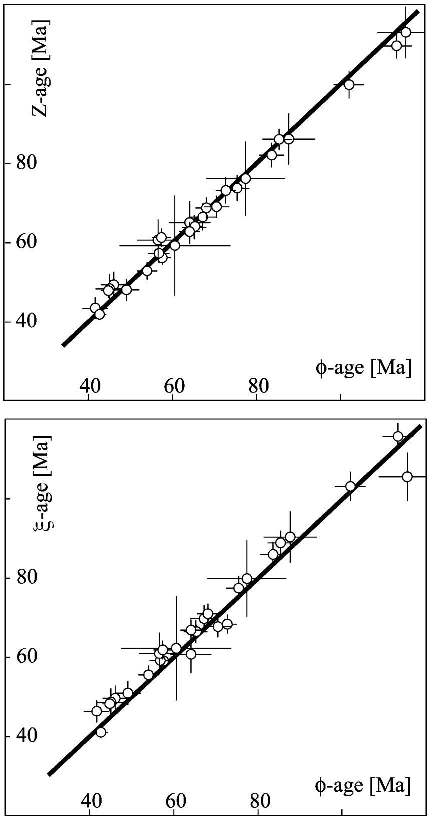

Fig. A1. The *Z*- and ξ-ages of the samples plotted against their independent ages (ϕ-ages). The good agreement provides a strong argument that the ages are accurate. The error bars represent 1σ statistical errors. The scatter of the data is less than suggested by the error bars because the same values for fossil (ρ_s) and induced track densities (ρ_i) were used in all age calculations.

0.01) are again different as a result of different track identification criteria. The dissimilar *R*- and ζ-factors of the two analysts reveal the magnitude of the effect of track identification criteria on AFT counts. The consistency of the ϕ-, *Z*- and ζ-ages, on the other hand, shows that they are adequately dealt with in both dating methods.

B.2. Track counting

The track counts were performed with a Leitz Aristomet microscope at a nominal magnification of 400 × , using transmitted light. The external detectors were repositioned, trackside down, on the apatite mounts, in the same position as during irradiation. Fossil tracks were counted by focusing on the apatite surface through the muscovite detector; induced tracks were counted by focusing on the underside of the external detector, without moving the microscope stage (Jonckheere and Wagner, 2000). This has practical advantages: (1) there is no need for reference points; in particular in standards, the mounds around the reference points tend to deteriorate the contact between the mount and external detector during later irradiations; (2) there is no need for motorized stages or for calibration before the track counts; (3) the positioning precision is high; thus, the analysis of grains with low induced track densities becomes more reliable; this proved an important practical advantage in the present study, because many samples have a low uranium content. Prismatic apatite surfaces were selected for the track counts. Whenever possible at least 20 grains were dated; all suitable grains were counted in samples that contained less than 20 grains.

B.3. Track length measurements

Track length measurements were performed at a nominal magnification of 2000 using a Calcomp Drawingboard II digitizer, a McIntosh computer, and Trevorscan software. At least 100 horizontal confined tracks parallel to prismatic surfaces were measured; all suitable tracks were measured in samples that contained less than 100. No distinction was made between TINTs and TINCLEs. Separate mounts were prepared for four samples (Y113, Y118; Y126; Y158) that had yielded sufficient apatite for additional track-length measurements. These mounts were irradiated with Cf-fission fragments by Donelick Analytical to increase the number of confined tracks (Donelick and Miller, 1991) and etched in 5.5 M HNO_3, so that the kinetic parameter D_{par} could be used in modeling their thermal histories (Donelick et al., 1999). No such information is available for the samples in which the confined track lengths were measured in the same mounts as used for dating.

B.4. Modeling the thermal histories

The thermal histories were modeled with AFT-Solve 1.1.3 (Ketcham et al., 2000). The annealing equations of Laslett et al. (1987) were selected when no compositional information was available. The equations of Ketcham et al. (1999) were selected for the Cf-irradiated samples, for which kinetic information was available through D_{par}. As a rule, 10.000 candidate temperature–time ($T[t]$) paths were generated by a Monte-Carlo process. Occasional, much longer runs confirmed that the solutions remained stable after 10.000 iterations. A Monte Carlo procedure was preferred because more efficient search algorithms are not well enough understood to exclude that they converge toward a local best-fit solution. No minimum or maximum heating or cooling rates were set because no such limits are imposed by the independent geological information. The segments connecting the nodes defining each $T[t]$-path were not subdivided. This has the effect that the number of degrees of freedom of the $T[t]$-path is limited to n, where n represents the number of free nodes. Because the number of free nodes is determined by the number of user-entered constraints, this procedure enabled us to discriminate between different $T[t]$-solutions by repeated modeling of a single sample with well-considered changes of the number and position of the constraints. This procedure showed that the selection of constraints has an important effect on the resulting $T[t]$-paths. In order to keep track of how the number and position of constraints affect the modeling results, we have consistently used the minimum number of constraints and modeled each sample several tens of times, gradually shifting their position. In this study, we have set a pair of initial and a pair of final constraints, adding up to three central constraints depending on the track length distribution.

Except through measurements of D_{par}, no compositional information was gathered for several reasons. First, most published apatite compositions are close to that of Durango apatite; compositional variations within this range have a moderate effect on track annealing kinetics (Ketcham et al., 1999, Fig. 8 and its discussion), which for our purposes are well enough described by the equations of Laslett et al. (1987). Second, the compositional control of annealing kinetics is not well enough understood. No linear combination of compositional parameters allows predicting track-annealing kinetics with confidence (Ketcham et al., 1999, p. 1251), so that the unconsidered use of simple compositional parameters is problematic. Third, the effect of apatite composition on the $T[t]$-paths is to shift the good-fit temperature ranges at the constraints up or down by 10 or, in extreme cases, tens of degrees. This effect is less important than that due to the number and position (in time) of the constraints. In this study, we have taken the latter effect into account as best as possible. To account for the lack of data and understanding of compositional effects, our interpretation is not based on the exact temperatures predicted by the modeling.

References

Allen, M.B., Macdonald, D.I.M., Xun, Z., Vincent, S.J., Brouet-Menzies, C., 1997. Early Cenozoic two-phase extension and late Cenozoic thermal subsidence and inversion of the Bohai Basin, northern China. Mar. Pet. Geol. 14, 951–972.

Angelier, J., 1984. Tectonic analysis of fault slip data sets. J. Geophys. Res. 89, 5835–5848.

Bellier, O., Vergély, P., Mercier, J., Ning, C., Deng, N., Yi, M., Long, C., 1991. Analyse tectonique et sedimentaire dans les monts Li Shan (province du Shanxi-Chine du Nord): datation des regimes tectoniques extensifs dans le graben de la Weihe. Bull. Soc. Geol. Fr. 162, 101–112.

Chen, Q., Dickinson, W.R., 1986. Contrasting nature of petroliferous Mesozoic–Cenozoic basins in eastern and western China. Am. Assoc. Pet. Geol. Bull. 70, 263–275.

Chen, H., Qin, D., 1989. Unstable cratonic and Paleozoic basins of China. In: Zhu, X. (Ed.), Sedimentary Basins of the World 1. Elsevier, Amsterdam, pp. 7–16.

Chen, F., Dai, S., Pan, G., 1989a. The Cretaceous–Paleogene salt-bearing basins in eastern China. In: Zhu, X. (Ed.), Sedimentary Basins of the World 1. Elsevier, Amsterdam, pp. 137–146.

Chen, W., Li, Q., Li, D., Wang, X., 1989b. Geochronological implications of K/Ar isotope system of fault gouge—a preliminary study. Phys. Chem. Earth 17, 17–23.

Cowan, G.A., Adler, H.H., 1976. The variability of the natural abundance of ^{235}U. Geochim. Cosmochim. Acta 40, 1487–1490.

De Corte, F., Moens, L., Jovannovic, S., Simonits, A., Dewispelaere, A., 1986. Applicability of the $1/E^{1+\alpha}$ epithermal spectrum representation and the effective resonance energy in NAA. Radioanal. Nucl. Chem. Artic. 102, 37–57.

Donelick, R.A., Miller, D.S., 1991. Enhanced TINT fission-track densities in low spontaneous track density apatites using Cf-252-derived fission fragment tracks—a model and experimental observations. Nucl. Tracks Radiat. Meas. 18, 301–307.

Donelick, R.A., Ketcham, R.A., Carlson, W.D., 1999. Variability of apatite fission-track annealing kinetics: II. Crystallographic orientation effects. Am. Mineral. 84, 1224–1234.

Dou, L., Song, J., Wang, Y., 1996. Chronology of formation of the northeastern Tan-Lu fault zone and its implications. Geol. Rev. 42, 508–512 (in Chinese with English abstract).

Enkelmann, E., 2001. The Tan-Lu fault zone at the eastern edge of the Dabie Shan (Eastern China): a view from fission-track thermochronology. Diploma thesis, TU Bergakademie Freiberg, 46 pp.

Faure, M., Marchandier, Y., Rangin, C., 1989. Pre-Eocene synmetamorphic structure in the Mindoro–Romblon–Palawan area, west Philippines, and implications for the history of southeast Asia. Tectonics 8/5, 963–979.

Fletcher, C.J.N., Fitches, W.R., Rundle, C.C., Evans, J.A., 1995. Geological and isotopic constraints on the timing of movement in the Tan-Lu Fault Zone, northeastern China. J. Southeast Asian Earth Sci. 11, 15–22.

Galbraith, R.F., 1990. The radial plot—graphical assessment of spread in ages. Nucl. Tracks Radiat. Meas. 17, 207–214.

Galliker, D., Hugentobler, E., Hahn, B., 1970. Spontane Kernspaltung von ^{238}U und ^{241}Am. Helv. Phys. Acta 43, 593–606.

Gilder, S., Keller, G.R., Luo, M., Goodell, P.C., 1991. Timing and spatial distribution of rifting in eastern China. Tectonophysics 197, 225–243.

Guedes, S., Hadler, J.C., Iunes, P.J., Paulo, S.R., Zuňiga, A., 2000. The spontaneous fission decay constant of U-238 using SSNTD. J. Radioanal. Nucl. Chem. 245, 441–442.

Hacker, B.R., Ratschbacher, L., Webb, L.E., McWilliams, M., Ireland, T., Calvert, A., Dong, S., Wenk, H.-R., Chateigner, D., 2000. Exhumation of the ultrahigh-pressure continental crust in east-central China: Late Triassic–Early Jurassic extension. J. Geophys. Res. 105, 13339–13364.

Han, J., Zhu, S., Xu, S., 1989. The generation and evolution of the Hehuai basin. In: Zhu, X. (Ed.), Sedimentary Basins of the World 1. Elsevier, Amsterdam, pp. 125–135.

Holden, N.E., 1995. Table of the isotopes (Revised 1995). In: Lide, D.R., Frederikse, H.P.R. (Eds.), CRC Handbook of Chemistry and Physics (76th edn.) CRC Press, Boca Raton, 11-38–11-143.

Holden, N.E., Holden, K.A., 1989. Reexamination of 2200 m/s cross section experiments for neutron capture and fission standards. Pure Appl. Chem. 61, 1505–1510.

Hoppes, D.D., Schima, F.J. (Eds.), 1982. Nuclear Data for the Efficiency Calibration of Germanium Spectrometer Systems. Natl. Bur. Stand., Washington, DC. Spec. Publ. No. 626, 146 pp.

Hu, J., Xu, S., Tong, X., Wu, H., 1989. The Bohai Bay basin. In: Zhu, X. (Ed.), Sedimentary Basins of the World 1. Elsevier, Amsterdam, pp. 89–105.

Jaffey, A.H., Flynn, K.F., Glemndenin, L.E., Bentley, W.C., Essling, A.M., 1971. Precision measurements of the half-lives and specific activities of ^{235}U and ^{238}U. Phys. Rev. C4, 1889–1906.

Jolivet, L., Maluski, H., Beyssac, O., Goffé, B., Lepvrier, C., Thi, P.T., Vuong, N.V., 1999. Oligocene–Miocene Bu Khang extensional gneiss dome in Vietnam: geodynamic implications. Geology 27, 67–70.

Jonckheere, R., 1995. Absolute age determination of apatite based on uranium fission-tracks: a methodical investigation. PhD Thesis, University of Gent, Belgium, 504 pp. (in Flemish).

Jonckheere, R., Wagner, G.A., 2000. A non-standard procedure for the analysis of external-detector samples introduced at the Heidelberg fission-track lab. Geol. Soc. Aust. Abstr. 58, 191–192.

Jonckheere, R., Van den haute, P., De Corte, F., Wagner, G.A., 2000. Fission-track [Age Calibration]. The next generation. Geol. Soc. Aust. Abstr. 58, 187–188.

Jovanović, S., De Corte, F., Simonits, A., Moens, L., Vukotić, P., Hoste, J., 1987. The effective resonance energy as a parameter in (n, γ) activation analysis with reactor neutrons. J. Radioanal. Nucl. Chem. 113, 177–185.

Ketcham, R.A., Donelick, R.A., Carlson, W.D., 1999. Variability of apatite fission-track annealing kinetics: III. Extrapolation to geological time scales. Am. Mineral. 84, 1235–1255.

Ketcham, R.A., Donelick, R.A., Donelick, M.B., 2000. AFTSolve: a program for multikinetic modeling of apatite fission-track data. Geol. Mater. Res. 2, 1–32.

Lapierre, H., Jahn, B., Charvet, J., Yu, Y., 1997. Mesozoic felsic arc magmatism and continental olivine tholeiites in Zhejiang Province and their relationship with the tectonic activity in southeastern China. Tectonophysics 274, 321–338.

Laslett, G.M., Green, P.F., Duddy, I.R., Gleadow, A.J.W., 1987. Thermal annealing of fission-tracks in apatite: 2. A quantitative analysis. Chem. Geol., Isot. Geosci. Sect. 65, 1–13.

Lin, W., Faure, M., Monié, P., Schärer, U., Zhang, L., Sun, Y., 2000. Tectonics of SE China: new insights from the Lushan massif (Jiangxi Province). Tectonics 19, 852–871.

Liu, J., Lin, C., Jiang, L., Chen, Z., 2000. Characteristics of Tertiary inversion structures and their influence on oil–gas accumulation in Xihu trough, East China Sea. Acta Geol. Sin. 21 (4), 350–355 (in Chinese with English abstract).

Ma, L., Yang, J., Ding, Z., 1989. Songliao Basin—an intracratonic continental sedimentary basin of combination type. In: Zhu, X. (Ed.), Sedimentary Basins of the World 1. Elsevier, Amsterdam, pp. 77–87.

Makovsky, Y., Klemperer, S.L., Ratschbacher, L., Alsdorf, D., 1999. Mid-crustal reflector on INDEPTH wide-angle profiles: an ophiolithic slab beneath the India–Asia suture in southern Tibet? Tectonics 18, 793–808.

Mughabghab, S.F., Divadeenam, M., Holden, N.E., 1981. Neutron cross sections. Neutron Resonance Parameters and Thermal Cross Sections: Part A. $Z=1$ to 60, vol. 1. Academic Press, New York, NY.

Northrup, C.J., Royden, L.H., Burchfiel, B.C., 1995. Motion of the Pacific plate relative to Eurasia and its potential relation to Cenozoic extension along the eastern margin of Eurasia. Geology 23 (8), 719–722.

Petit, J.-P., Proust, F., Tapponnier, P., 1983. Critères de sens de mouvement sur les miroirs de failles en roches non calcaires. Bull. Soc. Géol. France VII/25, 589–608.

Ratschbacher, L., Hacker, B.R., Webb, L.E., McWilliams, M., Ireland, T., Dong, S., Calvert, A., Chateigner, D., Wenk, H.-R., 2000. Exhumation of the ultrahigh-pressure continental crust in east-central China: Cretaceous and Cenozoic unroofing and the Tan-Lu fault. J. Geophys. Res. 105, 13303–13338.

Ratschbacher, L., Hacker, B.R., Calvert, A., Webb, L.E., Grimmer, J.C., McWilliams, M., Dong, S., Hu, J., submitted for publication. Tectonics of the Qinling belt (Central China): Subdivision, geochronology, and deformation kinematics. Tectonophysics.

Reiners, P.W., Zhou, Z., Xu, C., Ehlers, T., 2001. Zircon and apatite (U–Th)/He thermochronology of the Dabie Shan, China. Abstract, GSA annual meeting.

R.G.S. Anhui, 1975. 1: 200,000, Regional Geology of Anhui Province (in Chinese). Geological Publishing House, Beijing.

R.G.S. Anhui, 1987. 1: 500,000, Regional Geology of Anhui Province (in Chinese). Geological Publishing House, Beijing.

R.G.S. Hubei, 1990. 1: 500,000, Regional Geology of Hubei Province (in Chinese). Geological Publishing House, Beijing.

Roddick, J.C., 1978. The application of isochron diagrams in $^{40}Ar-^{39}Ar$ dating: a discussion. Earth Planet. Sci. Lett. 41, 233–244.

Roger, F., Tapponnier, P., Arnaud, N., Schärer, U., Brunel, M., Xu, Z., Yang, J., 2000. An Eocene magmatic belt across central Tibet: mantle subduction triggered by the Indian collision? Terra Nova 12 (3), 102–108.

Schmid, J.C., Ratschbacher, L., Hacker, B.R., Gaitzsch, I., Dong, S., 1999. How did the foreland react? Yangtze foreland fold-and-thrust belt deformation related to exhumation of the Dabie Shan ultrahigh-pressure continental crust (eastern China). Terra Nova 11 (6), 266–272.

Searle, M., Corfield, R.I., Stephenson, B., McCarron, J., 1997. Structure of the North Indian continental margin in the Ladakh-Zanskar Himalayas: implications for the timing of obduction of the Spontang ophiolite, India–Asia collision and deformation events in the Himalaya. Geol. Mag. 134, 297–316.

Spang, J.H., 1972. Numerical method for dynamic analysis of calcite twin lamellae. Bull. Geol. Soc. Am. 83, 467–472.

Sperner, B., Ratschbacher, L., Ott, R., 1993. Fault-striae analysis: a TURBO PASCAL program package for graphical presentation and reduced stress tensor calculation. Comput. Geosci. 19, 1361–1388.

Tapponnier, P., Molnar, P., 1977. Active faulting and tectonics in China. J. Geophys. Res. 82, 2905–2930.

Tong, W.X., Tobisch, O.T., 1996. Deformation of granitoid plutons in the Dongshan area, southeast China: constraints on the physical conditions and timing of movement along the Changle-Nanao shear zone. Tectonophysics 267, 303–316.

Turner, F.J., 1953. Nature and dynamic interpretation of deformation lamellae in calcite of three marbles. Am. J. Sci. 251, 276–298.

Van den haute, P., Jonckheere, R., De Corte, F., 1988. Thermal neutron fluence determination for fission-track dating with metal activation monitors: a re-investigation. Chem. Geol., Isot. Geosci. Sect. 73, 233–244.

Wang, Z., Lu, H., 2000. Ductile deformation and $^{40}Ar/^{39}Ar$ dating of the Changle-Nanao ductile shear zone, southeastern China. J. Struct. Geol. 22, 561–570.

Wang, Y., Jiang, L., Yang, W., 2000. Kinematical analysis on faults in the Lishui-Jiaojiang sag. Sci. Geol. Sin. 35 (4), 441–448 (in Chinese with English abstract).

Webb, L.E., Hacker, B.R., Ratschbacher, L., Dong, S., 1999. Thermochronologic constraints on deformation and cooling history of high- and ultrahigh-pressure rocks in the Qinling–Dabie orogen, eastern China. Tectonics 18, 621–638.

Wendt, I., Carl, C., 1991. The statistical distribution of the mean squared weighted deviation. Chem. Geol. 86, 275–285.

Xu, J., Zhu, G., 1995. Tectonic models of the Tan-Lu Fault Zone, Eastern China. Int. Geol. Rev. 36, 771–784.

Yin, A., Nie, S., 1993. An indentation model for the North and South China collision and the development of the Tanlu and Honam fault systems, eastern Asia. Tectonics 12, 801–813.

Zhang, Y., Wei, Z., Tao, R., Chen, R., 1989. The North Jiangsu–South Yellow Sea basin. In: Zhu, X. (Ed.), Sedimentary Basins of the World 1. Elsevier, Amsterdam, pp. 107–123.

Zhang, Y., Vergély, P., Mercier, J., 1995. Active faulting in and along the Qinling Range (China) inferred from SPOT imagery analysis and extrusion tectonics of south China. Tectonophysics 243, 69–95.

Zhang, Y., Vergély, P., Mercier, J., Wang, Y., Zhang, Y., Huang, D., 1999. Kinematic history and changes in the tectonic stress regime during the Cenozoic along the Qinling and southern Tanlu fault zone. Acta Geol. Sin. 73 (3), 264–274.

Zheng, X., 1985. Meso-Cenozoic volcanic rocks in east China and adjacent areas with relation to plate tectonics. Tectonophysics 112, 533–550.

Zhou, Z.Y., Seward, D., Qian, J., Lao, Q., 2000. Preliminary apatite fission-track analysis on Meso-Cenozoic sedimentary rocks from north Jiangsu Basin, China. 9th International Conference on Fission-track Dating and Thermochronology. Geol. Soc. Austr. Abstr. 58, 357–359.